UNIVERSITY *of* York

Achieving a Robust Grassy-ELM Operation Regime in CFETR

Yi-Ren Zhu[1], Ze-Yu Li[2,6], V. S. Chan[3,6], Jia-Le Chen[4], Xiang Jian[1], B. D. Dudson[5], A. M. Garofalo[6], P. B. Snyder[6], Xue-Qiao Xu[7], G. Zhuang[3] and CFETR physics team

[1]*State Key Laboratory of Advanced Electromagnetic Engineering and Technology, Huazhong University of Science and Technology, Wuhan 430074, China*

[2]*State Key Laboratory of Nuclear Physics and Technology, School of Physics, and Fusion Simulation Center, Peking University, Beijing 100871, China*

[3]*Department of Engineering and Applied Physics, School of Physical Sciences, University of Science and Technology of China, Hefei Anhui, 230026, China*

[4]*Institute of Plasma Physics, Chinese Academy of Sciences, Hefei, 230031, China*

[5]*York Plasma Institute, University of York, Heslington, York, YO10 5DD, UK*

[6]*General Atomics, San Diego, CA,92186, USA*

[7]*Lawrence Livermore National Laboratory, Livermore, CA94550, USA*

Corresponding Author: gezhuang@ustc.edu.cn, chanvs@ustc.edu.cn

Abstract

We have identified a robust grassy-ELM operation regime for future tokamak reactors. The regime exists within a pedestal top electron collisionality (ν^*) window at high global poloidal beta (β_p). The existence of an upper ν^* limit for grassy-ELMs is consistent with results previously reported in experiments [N. Oyama et al 2010 Effects of edge collisionality on ELM characteristics in the grassy ELM regime Nucl. Fusion 50 064014], while the existence of a lower ν^* limit has not been reported previously. Using EPED and BOUT++, a theoretical model that quantitatively explains the physics of the grassy-ELMs within the window, which distinguishes them from the small mixed-ELMs at lower ν^*, is presented for the first time. A peeling-ballooning stability boundary is obtained by scanning the operating density space. The change in density corresponds to a change in ν^* that affects the pedestal bootstrap current. High β_p leads to a strong Shafranov shift, which affects the flux surface averaged pressure drive. The two effects combine to create a peeling-dominated window in intermediate ν^* buffered by ballooning-dominated regimes. Only the peeling-dominated regime shows a cyclic behavior in the perturbed pressure during the nonlinear simulation of an ELM crash, reminiscent of grassy-ELM dynamics. Similarly, the energy released across the separatrix is demonstrated to be significantly smaller. The quick recovery of the ELM crash is explainable by the rapid rise of a low n kink-peeling instability when the pedestal current I_{ped} exceeds a threshold at high β_p. It minimizes the excursion beyond marginal stability and is absent in the ballooning-dominated

regime. Comparison with recent experiments over a range of β_p and ν^* strongly supports the physical picture proposed by the modeling.

Key words: Grassy-ELMs, collisionality, high β_p, peeling-ballooning mode, CFETR, experimental comparison.

1. Introduction

Identifying stable operation regimes with high performance and acceptable heat and particle control is a key challenge for tokamak fusion reactors. China Fusion Engineering Test Reactor (CFETR) is being proposed as the next-generation fusion facility in China[1], which aims to bridge the technological gaps between ITER[2] and a fusion demonstration reactor (DEMO). The main mission of CFETR includes: demonstrating high fusion energy production; demonstrating tritium self-sufficiency with target tritium breeding ratio (TBR) > 1; exploring options for DEMO blankets and divertor solutions; and developing solutions for easy remote maintenance of in-vessel components and material integrity[3]. With the initiation of the engineering design phase of CFETR, a method to control Edge Localized Modes (ELM), compatible with the desired operating scenarios and engineering constraints, is a major challenge. ELMs are repetitive MHD instabilities at the plasma edge and could lead to a rapid loss of energy and particles from the plasma edge that potentially shortens the lifetime of first wall materials and decreases the confinement time of a tokamak[4]. Resonant Magnetic Perturbation (RMP) using 3D coils to reduce ELM amplitude has demonstrated success in some ITER relevant conditions within a low edge safety factor (q_{95}) window[5]. However, CFETR is designed to operate at high q_{95} to enhance the bootstrap current for steady-state operation. Although recent results suggest that RMPs could be extended to higher q_{95}[6], they are still preliminary and we have to wait for further experimental confirmation. Another issue is that neutron shielding demands that the RMP coils be placed behind the tritium breeding blankets, which results in high coil current requirement. Other ELM control methods, such as injection of small pellets[7], are still in early stages of development. This study explores the

1   possibility of operating with benign ELMs that are compatible with high core performance and

2   effective edge plasma exhaust solutions.

3   The accessibility of high-performance H-mode with small or no ELMs is an essential

4   requirement for the design of viable operation scenarios for CFETR. Type-I ELMs[8] with large

5   periodic bursts are of serious concern, because they can eject over 10% of the pedestal stored

6   energy to the first wall in a very short time. They are believed to be triggered by peeling-

7   ballooning (PB) instabilities[9] driven by high edge pressure and current, and must be avoided

8   in CFETR operation. Type-II ELMs observed in AUG, TCV[10] and JET in highly shaped

9   plasmas[11] have smaller amplitudes compared with Type-I ELMs and show no detectable stored

10 energy drop or heat flux increase at the divertor target[12][13]. However, Type-II ELMs occur

11 only at high edge ν^*, which is incompatible with CFETR steady-state scenarios. Type-III ELMs

12 also have small amplitudes. They are transient oscillations that typically occur at the initial

13 phase of an L-H transition as the heating power is being ramped up[4]. They exist over a range

14 of collisionalities[14] and occur below the ballooning stability limit. For other edge conditions,

15 data for access to quiescent H-mode (QH) [15] is still preliminary, while I-mode [16] has an L-

16 mode particle edge and may not be compatible with high H_{98}, high bootstrap fraction operation.

17 A good candidate for CFETR is the grassy-ELM regime at moderate ν^* first observed in the

18 JT60-U tokamak[17], which is characterized by a high frequency and localized, periodic

19 collapses of the pedestal. The transient heat load on the first wall from the grassy ELMs is

20 manageable and they also favorably cleanse the plasma of edge impurities.

21   According to experiments[17], grassy ELMs exist within an intermediate ν^* window in the

22 pedestal at high β_p . Whether grassy-ELM operation is a viable solution for CFETR critically

23 depends on identifying a robust ν^* window and determining if it is compatible with both a high-

24 performance core and a divertor solution. Since the core parameters affect the profile of the

25 pedestal, any quantitative approach to answer this question has to begin with a core-pedestal

26 consistent equilibrium. This equilibrium is employed in a linear stability analysis to search for

27 and relate the most unstable modes to the pedestal characteristics along the marginal PB

28 stability boundary. We use this information to identify the dominant instability drive

29 mechanism. A nonlinear simulation links the ELM dynamics, i.e. the crash behavior, to the

30 nature of the unstable mode, which depends on ν^* and β_p. A combination of linear and

nonlinear analyses elucidates the physics involved in triggering a repetitive ELM cycle, and quantifies a ν^* window with robust grassy-ELMs for CFETR operation. Finally, the predicted features of the ELM behavior are compared with more recent experimental data. Specifically, we check the change in ELM characteristics, the most unstable mode in the linear phase, and the fraction of ejected energy during an ELM burst over a range of β_p and ν^*.

The organization of this paper is as follows. In Section 2, we construct a series of self-consistent equilibria by applying a core-pedestal coupling simulation workflow to obtain the CFETR plasma profiles. In Section 3, linear stability analysis using EPED is used to characterize in details the most unstable modes along the PB stability boundary at the pedestal of CFETR. In Section 4, nonlinear simulations of the unstable mode evolution and the perturbed pedestal pressure for different values of ν^* using BOUT++ are presented. A link between the instability mechanisms and the ELM dynamics is developed. Parameter spaces of predicted Type-I ELMs and grassy-ELMs, as well as their distinguishing features, are benchmarked with experiments from DIII-D in Section 5. In Section 6, the results are summarized and extension to future studies is discussed.

2. Self-consistent equilibrium construction

The first step of performing a reliable edge stability analysis is to construct a self-consistent equilibrium. Previously, starting with a baseline case for CFETR[18], we used the EFIT code alone to construct a series of equilibria with different pedestal parameters[19] to model the changing pedestal boundary conditions. This fitting method unphysically decouples the pedestal pressure gradient α_{ped} and current I_{ped} as they are varied. In reality, α_{ped} $\left(-\frac{\mu_0}{2\pi^2}\frac{\partial p}{\partial \psi}\frac{\partial V}{\partial \psi}\left(\frac{V}{2\pi^2 R_0}\right)^{1/2} \right)$ and I_{ped}(the integrated pedestal current) are strongly coupled through the pedestal bootstrap current, which has to be accounted for. In addition, it is now well-accepted that the pedestal sits approximately at marginal stability to PB modes[20] for Type I ELMs discussed in this paper and the marginal stability condition is strongly influenced by the core equilibrium parameters. To account for these two factors, a self-consistent workflow shown in Fig. 1 for CFETR is employed to generate equilibria that represent the entire plasma, following a method previously developed by O. Meneghini [21]. Key steps of the workflow are

described below.
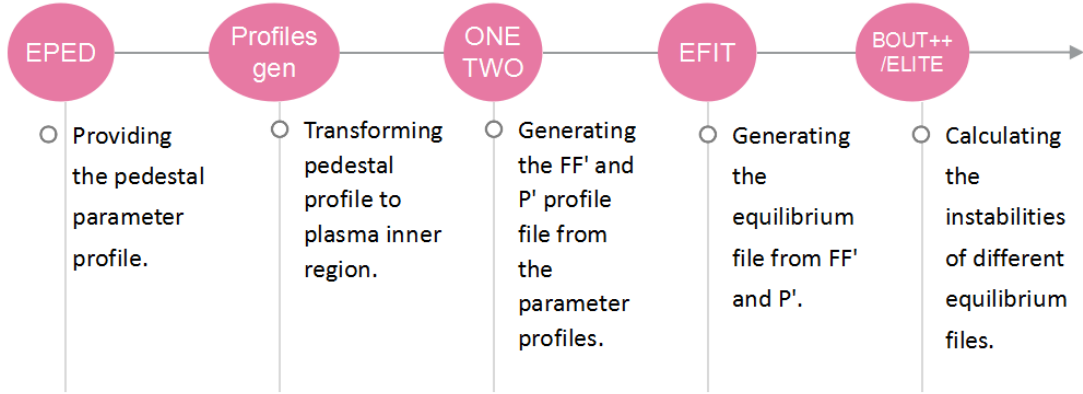
Figure 1. *Workflow of constructing self-consistent CFETR equilibrium*

2.1 The EPED pedestal model

The EPED model was developed for predicting the pedestal height and width in H-mode, and has been extensively validated with many experiments [22][23][24]. Combining the physics of peeling-ballooning mode (PBM) constraint and the kinetic-ballooning mode(KBM) constraint, EPED proceeds through a series of code modules, including the equilibrium construction code TOQ[25], the eigenvalue stability analysis code ELITE[20], and the 'ballooning critical pedestal'(BCP) technique[23]. In EPED, TOQ starts with a given set of core and pedestal plasma 0D parameters to generate a series of equilibria with different pedestal structures. ELITE is a code based on peeling-ballooning theory, and can calculate both growth rates and mode structures of the ideal linear instabilities[26]. With highly efficient calculation of a chosen set of modes, within a large range of toroidal mode numbers, ELITE can scan through the equilibria produced by TOQ, to yield a PB marginal stability constraint in pedestal width and height space.

Similarly, the BCP technique is used to calculate the KBM constraint,

$$\Delta_{\psi_N} = \beta_{p,ped}^{1/2} G(\nu^*, \varepsilon, \dots) \tag{1},$$

in the same parameter space. The intersection of the PB and KBM constraints thus calculated yields a unique, predictive pedestal height and width for a given set of core/pedestal 0D parameters. As illustrated in Fig. 7 of Ref. [24], EPED expresses the intersection of the calculated PB and KBM constraints as the maximum values of pedestal height and width at marginal stability for a fixed set of pedestal density and Z_{eff}. The intersecting pedestal height

1 and width will change as the pedestal density is varied (keeping Z_{eff} fixed for this study). Thus,

2 by varying the pedestal density from low to high, a complete marginal stability boundary to PB

3 and KBM mode in pedestal height and width space can be mapped out, with which the pedestal

4 profile can be constructed for any chosen density or ν^*.

5 *2.2 Core-pedestal coupling: OMFIT*

6 A platform called One Modeling Framework for Integrated Tasks (OMFIT) is developed to

7 enable physics codes to interact in complicated workflows through efficient data-passing[27].

8 By coupling EPED, TGYRO[28], ONETWO[29] and EFIT[30] with OMFIT, we could model the

9 iterative interaction between the core and the pedestal, i.e. changing the pedestal profile can

10 affect the core equilibrium, and vice versa. EPED mainly focuses on providing a reliable profile

11 that reflects the physics at the boundary region, while TGYRO is used in our workflow to

12 realize a compatible, fully-evolved kinetic profiles in the core region. TGYRO is a transport

13 solver which computes the transport fluxes of energy, particle, and toroidal angular momentum

14 induced by turbulent and neoclassical transport. Only electrostatic ITG, TEM and ETG

15 turbulence are considered in our simulation. Fast particles are included in the kinetic

16 reconstruction and both helium and trace argon impurities are accounted for. By matching the

17 transport fluxes with the integrated sources and sinks from ONETWO, one can obtain the

18 steady-state profiles of temperature, density and toroidal rotation from the center out to a point

19 typically around $\rho=0.8$. A transition region which connects the pedestal top and core is

20 introduced to speed up the TGYRO convergence process. The region is constructed by a linear

21 extrapolation of the gradients between the top of the pedestal and the starting point of the

22 TGYRO core simulation. This ensures a smooth transition up to the first derivatives of the

23 kinetic profiles. The combined profile is shown in Fig. 2.

1
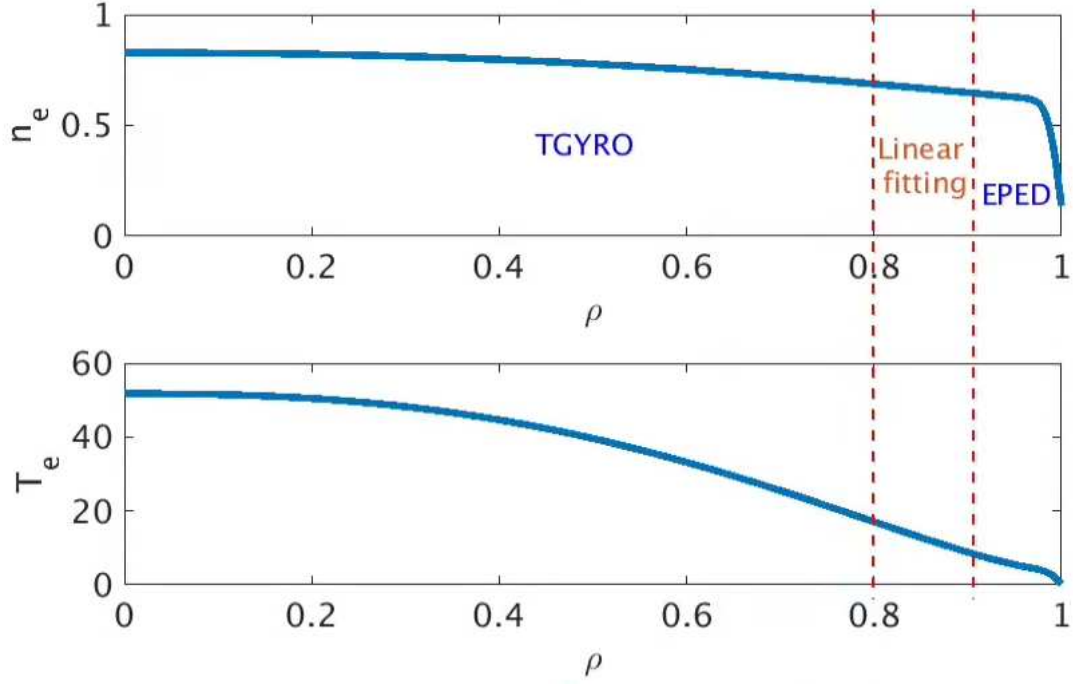
Figure 2. Illustration of radial connectivity of core, transition and pedestal region in CFETR

self-consistent workflow, plotted as a function of the normalized poloidal flux ρ. EPED provides

the pedestal profile, linear fitting equation extends the pedestal parameters to the core pivot

point, with which TGYRO calculates the core profiles($n_e(10^{20}m^{-3})$, $T_e(keV)$).

The transition region allows the gradient scale lengths that are consistent with the transport

calculation in the core to smoothly connect to the values that are consistent with the PB and

KBM dynamics of the pedestal. We note that with the change of the core kinetic profiles, the

plasma current profile as well as the core equilibrium will also change. The last piece of work

to ensure self-consistency is to update the steady-state plasma current profile with the given

kinetic profiles and generate a new equilibrium. This is carried out using

ONETWO/TGYRO/EFIT. Specifically, the total current is fixed by the physics design. When

the core kinetic profiles are changed, we have to go through an iterative loop of

ONEWTO/TGYRO/EFIT including the adjustment of auxiliary current drive power to maintain

the same current. The core current profile is determined by a combination of bootstrap current

and auxiliary current drive, which depend on the kinetic profile and equilibrium. The loop has

to be iterated until convergence.

2.3 ONETWO-EFIT convergence loop

1   The ONETWO transport code is used for two essential functions in our workflow. The first

2   is, using an input equilibrium and kinetic profiles, ONETWO calculates all the sources and

3   sinks required to maintain the particle, temperature and current profiles. The sources and sinks

4   are used as input to TGYRO for calculating any changes in the kinetic profiles. The second

5   function of ONETWO is to take the updated kinetic profiles and evolve the current profile to a

6   new steady-state. The result is then used by EFIT to compute a new equilibrium. Both function

7   1 & 2 are iteratively repeated with TGYRO until convergence is achieved, and a fully self-

8   consistent equilibrium, including the pedestal predicted by EPED, is obtained as shown in Fig.

9   3. The self-consistency is crucial for our nonlinear BOUT++ study since low-n PB modes have

10   finite width and can extend inward of the top of the pedestal. The pressure gradient near the top

11   of the pedestal can sensitively affect the ballooning drive. In particular, as we shall discuss later,

12   it is the flux surface averaged pressure that drives the ballooning instability, hence the global

13   equilibrium including an accurate Shafranov shift is critical. Although BOUT++ cannot use

14   this equilibrium directly, pressure and current profiles from the gfile generated by EFIT can be

15   easily converted to BOUT++ grid files, and similarly density and temperature profiles used by

16   BOUT++ are extracted from the pfile in ONETWO output.

17
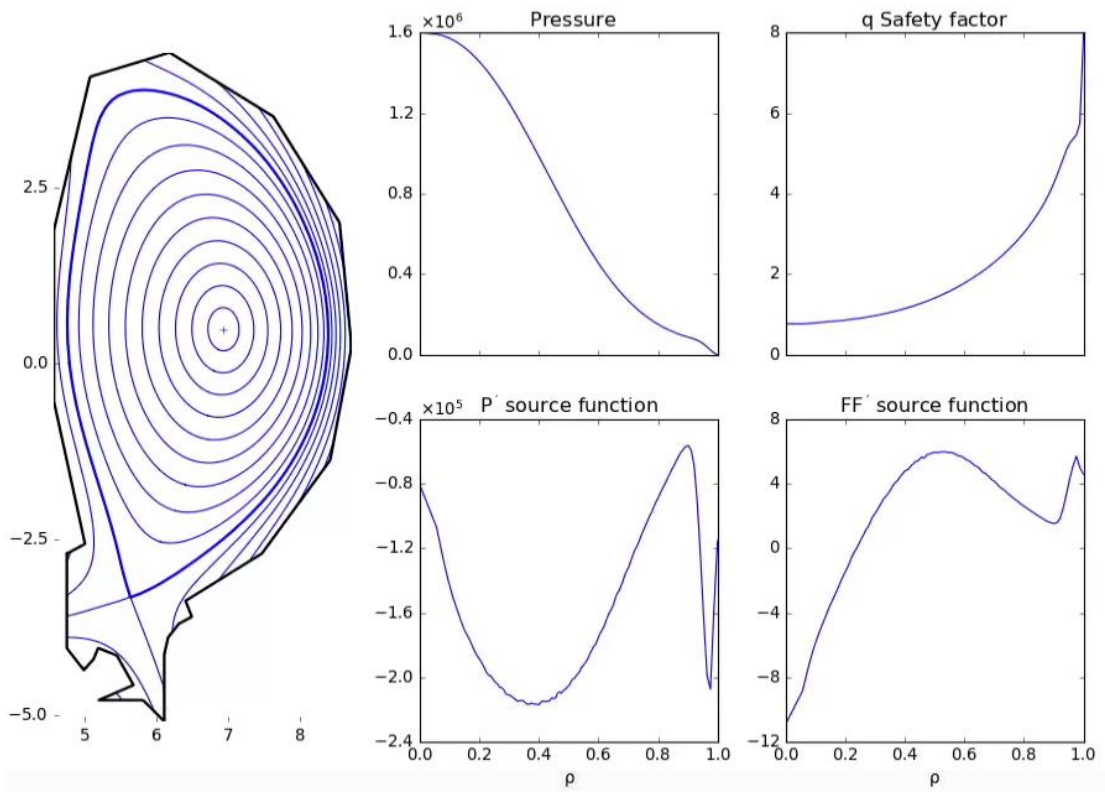
***Figure 3.** Equilibrium of CFETR R=6.6m phase II baseline scenario, following convergence to a self-consistent state. Equilibrium profiles of pressure and safety factor are shown along with the sources calculated using ONETWO[31].*

## 3. Linear stability analysis of marginally stable operation scenarios

3.1 Pedestal parameters scan and peeling ballooning boundary of CFETR

Based on the CFETR R=6.6m phase II baseline case shown in Table 1 and starting at a low n_{e_ped}, EPED is used to compute the pedestal width and height at marginal PB stability subject to KBM constraint as described in Section 2. This is continued as the density is increased until the entire density range is mapped out. The resultant PB boundary of CFETR in any combination of the set (I_{ped}, α_{ped}, pedestal height, pedestal width) can be displayed. As an example, the pressure gradient α_{ped} and edge current I_{ped} ($\equiv J.B/B0$)parameter space is shown in Fig. 4(a). Following convention, the upper boundary is usually called the peeling boundary and the lower boundary is called the ballooning boundary. However, as we shall see, the dominance of peeling and ballooning drive can vary along the upper boundary, and that can affect the physics in an important way. We note the familiar feature that with increasing density, the maximum edge current and pedestal pressure gradient increase in locked steps on the upper branch, but when the pedestal top density n_{e_ped} is beyond a threshold value of about $2.2 \times 10^{20} \text{m}^{-3}$ they start to decrease, again in locked steps, along the lower branch. This trend is consistent with the direct proportionality of the bootstrap current with rising pressure gradient. However, increasing density does not necessarily correspond to increasing pressure gradient along the marginal stability boundary, which is dictated by the instability drive that sets the limit. In general, peeling modes (with lower toroidal mode numbers n) are the limiting instability at high edge current and ballooning modes (with higher n numbers) are most unstable at high pressure gradient. Intermediate n (~10), coupled peeling-ballooning modes are the limiting instability when current and pressure gradient drives are comparable.

***Table 1.** EPED input parameters of CFETR R=6.6m phase II scenario*

Parameters	CFETR Phase II

Ip(MA)	10.0
B(T)	6.0
R(m)	6.6
a(m)	1.8
Elongation	2.0
Triangularity	0.50
$n_{e\_ped}(10^{19}\ m^{-3})$	3-30
Global β_N	3.14-3.4
Z_{eff_ped}	1.8
A_ion	2.5
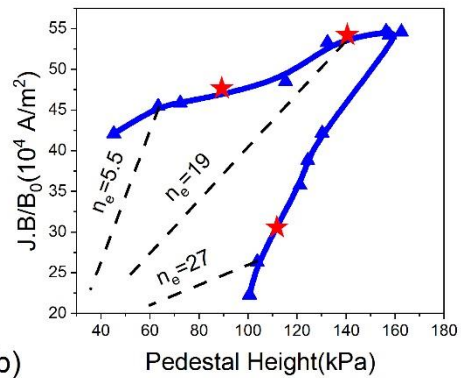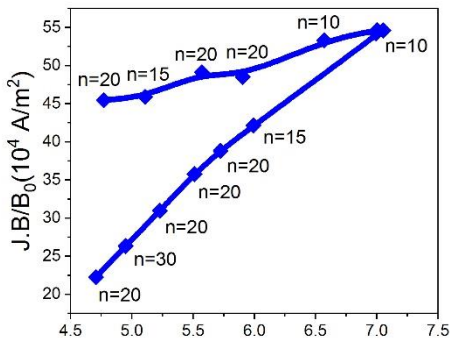
1 (a) (b)

2 **Figure 4.** *Peeling-ballooning boundary of CFETR R=6.6m phase II in (a) J.B/B_0 versus α_{ped}*

3 *space obtained from density scan in EPED , and (b) J.B/B_0 versus pedestal height space. The*

4 *density is scaled by $10^{19}\ m^{-3}$.*

5   Fig. 4(b) shows the same case as in Fig. 4(a) for CFETR R=6.6m but with the pressure

6 gradient in the horizontal axis replaced by the pedestal height. For a fixed density, the pedestal

1   current J.B/B0 is approximately linearly proportional to the pedestal height using a simple

2   fitting from EPED[see Fig. 5(b) in Ref.33]:

3      $J.\frac{B}{B0} = (0.8328 - 0.0229 n_e) P_{ped}$ (2)

4   Hence the intersection of each dashed line with the PB boundary represents a different density,

5   going from low density in the peeling branch to high density in the ballooning branch.

6   Furthermore, we can relate the density with the collisionality ν^* using the formula[32]

7      $\nu^* = 6.921 \times 10^{-18} \frac{R q_{95} n_e Z_{eff} \ln \Lambda_e}{\varepsilon^{3/2} T_e^2}$ (3)

8   Combining the information provided by Fig. 4(a) & (b) and Eqs.(2) and (3) , we can derive

9   three relations: pedestal height versus collisionality/density, J.B/B0 versus collisionality, and

10   pedestal gradient versus collisionality, as shown in Fig. 5 (a)-(c), that are crucial for our search

11   for the grassy ELM window and understanding of the physics leading to grassy-ELMs.

12

13
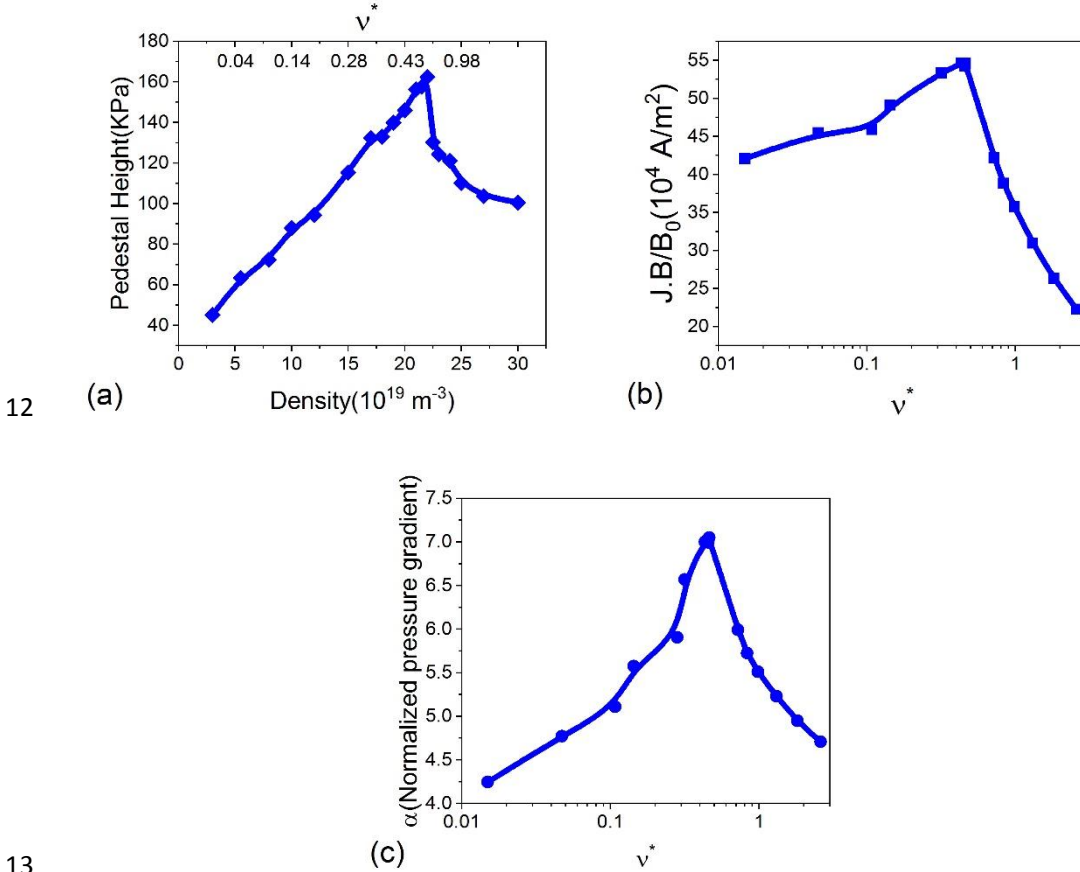
14 **Figure 5.** *Plot of (a) pedestal height versus density; (b) J.B/B₀ versus electron collisionality;*

15 *and (c) pressure gradient versus electron collisionality.*

16

17 *3.2 Identifying Peeling and Ballooning Dominant Regions*

Fig. 5(a) clearly shows a trend of rising pedestal height with density, reaching a peak at some intermediate density, after which it starts to decline. This trend is consistent with published experimental observations[33]. Note that the density at the peak sometimes corresponds to a transition to the so-called super H-mode[33] at higher density, which we are not considering in this study. Fig. 5(b) shows a similar trend of rising pedestal current $J.B/B_0$ with increasing collisionality, reaching a peak that approximately corresponds to the maximum pedestal height in Fig. 5(a). Beyond this point, $J.B/B_0$ drops rapidly with collisionality. Clearly, the kink-peeling drive coming from the pedestal current is largest at this point. To determine whether it is the dominant mechanism, we need to compare it with the ballooning drive due to the pressure gradient, which also shows a peak in the same proximity [Fig. 5(c)]. The resolution comes from recognizing that in ballooning mode theory, it is the flux-surfaced averaged pressure gradient $< \kappa \cdot \nabla P >$ that enters in the calculation of the growth rate[34]. In other words, the effective pressure gradient comes from the average of the good-curvature and bad-curvature regions. This is particularly important at high β_p[32], such as for CFETR with $\beta_p \sim 2$. The strong Shafranov shift at high β_p enhances the good-curvature weighting leading to a reduced flux-surface averaged pressure gradient drive. Indeed, the $< \kappa \cdot \nabla P >$curve in Fig. 6 looks very different from the local ∇P curve. Instead of a peak, the $< \kappa \cdot \nabla P >$ curve shows a minimum at the same ν^* location. Note that Fig. 6 only illustrates the beneficial effect of averaging over good/bad curvature for high β_p plasma. The actual ballooning drive is proportional to $< \kappa \cdot \nabla P |X| >$ where $|X|$ is the perturbed mode radial width along the flux surface. If $|X|$ is weighted heavily on the bad curvature side, the ballooning drive is positive, i.e. destabilizing. That is why lower n modes benefit more from the flux surface averaged good curvature effect. We also examine the most unstable mode spectrum at ν^*=0.39 (Fig.7(b)) using BOUT++ 3-field ELM-PB model, which shows a peak at lower n, compared with that at ν^*=0.14 (Fig.7(a)) and ν^*=1.31 (Fig.7(c)). The low-n modes make the stabilizing effect of the good-curvature more effective, resulting in a strong suppression of $< \kappa \cdot \nabla P >$ compared with the I_{ped} drive. All these evidence support the conclusion that kink-peeling drive rather than ballooning drive dominates near the peak of the pedestal height. At high ν^*, pressure gradient drive clearly dominates and intermediate-n ballooning modes occupy the most unstable spectrum as shown in Fig. 7(c). At low ν^*, both current and pressure gradient drives are weak, so it is harder to ascertain without

1   quantitative evaluation which one is more dominant. Since ballooning mode width is narrower,

2   it might be more likely for a high-n ballooning mode at the pedestal top, where diamagnetic

3   stabilization is weakest, to become unstable first. This has been reported in a previous study[19]

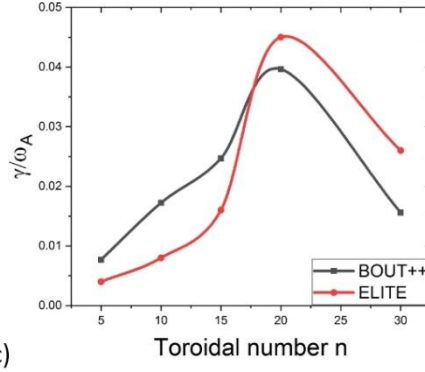4   and the most unstable mode spectrum in our case (Fig.7(a)) also supports that.
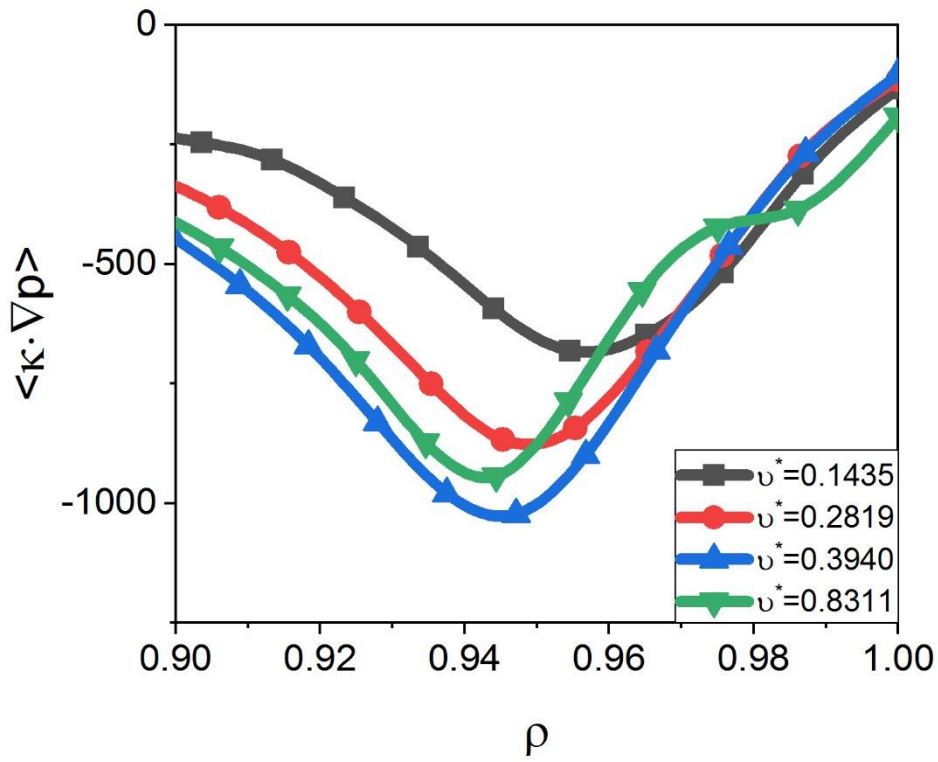
5

6   *Figure 6. The flux-surfaced averaged pressure gradient drive for different collisionalities.*
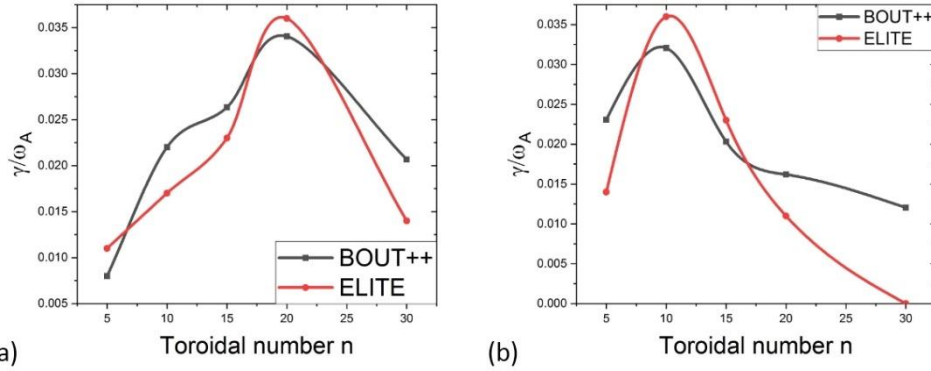
Figure 7. Unstable mode spectrum computed by BOUT++ at (a) low collisionality (v^*=0.14), (b)intermediate collisionality (v^*=0.39) and (c) high collisionality (v^*=1.31). The black curves are from BOUT++ and the red curves are from ELITE.

From linear analysis using EPED and BOUT++ with self-consistent equilibria, we have demonstrated that the three important quantities (pedestal height, $J.B/B_0$ and pressure gradient), which characterize a stable pedestal, are sensitive functions of the pedestal v^*. There is an intermediate v^* window where the instability is dominated by kink-peeling drive. Outside of this window, ballooning drive is significant and possibly dominant. How this characteristic impacts the nonlinear behavior of the modes and the ELM dynamics is the focus of our study in Section 4. Before leaving this Section, we should point out from the KBM constraint that the pedestal width is proportional to $\beta_{p\_ped}^{1/2}$, hence the width is broadest at maximum pedestal height. This combines with the unstable low-n peeling modes has some important consequences on the ELM dynamics as we shall discuss.

4. Nonlinear simulation of ELM behavior using BOUT++ 3-fields model

In Section 3, we have identified three different v^* regimes along the PB stability boundary of CFETR with different pedestal properties, which lead to different unstable mode

1 characteristics. For detail understanding of ELM behavior, nonlinear simulation is needed to

2 analyze the evolution of plasma profiles including the consideration of coupling effects from

3 multiple unstable modes. Since PB modes are believed to be responsible for ELMy behavior in

4 H-mode[35], the next step is to explore how the ELM dynamics might change as ν^* increases

5 from low to high values. We pick one representative point in each regime to study, and they are

6 indicated by red stars in Fig. 4(b). The properties of each case are given in Table 2. The

7 calculation is carried out in the BOUT++ two-fluid three-fields framework[36], which allows us

8 to simulate the nonlinear dynamics of ELMs beyond linear MHD physics. Only the short time

9 scale (~ a few hundred τ_A time) ELM crash phase is studied. The long transport time-scale

10 recovery phase is excluded because of the absence of a realistic pedestal heat source in this

11 BOUT++ model. A minimum set of nonlinear equations describing the temporal evolution of

12 the perturbed magnetic vector potential $\tilde{A}_\parallel$, vorticity ϖ and pressure $\tilde{p}$ can be extracted from

13 a more complete set of the BOUT two-fluid three-fields equation, with an added effect of hyper-

14 resistivity incorporated[36]. These equations are written as:

15
$$\frac{\partial \tilde{\varpi}}{\partial t} + v_E \cdot \nabla \tilde{\varpi} = B_0 \nabla_\parallel \tilde{J}_\parallel + 2b_0 \times \kappa_0 \cdot \nabla \tilde{p} + \mu_{i,\parallel} \partial_{\parallel 0}^2 \tilde{\varpi} + \mu_{i,\perp} \nabla_\perp^2 \tilde{\varpi} \tag{4}$$

16
$$\frac{\partial P}{\partial t} + v_E \cdot \nabla P = \chi_\parallel \partial_{\parallel 0}^2 P \tag{5}$$

17
$$\frac{\partial \tilde{A}_\parallel}{\partial t} = -\nabla_\parallel \Phi + \frac{\eta}{\mu_0} \nabla_\perp^2 \tilde{A}_\parallel - \frac{\eta_H}{\mu_0} \nabla_\perp^4 \tilde{A}_\parallel \tag{6}$$

19
$$\tilde{\varpi} = \frac{n_0 M_i}{B_0} (\nabla_\perp^2 \tilde{\phi} + \frac{1}{n_0 Z_i e} \nabla_\perp^2 \tilde{p}_i), \Phi = \tilde{\phi} + \Phi_0,$$

18 with $P = \tilde{p} + P_0$ in the above equations $\hspace{4cm}$ (7)

20
$$J_\parallel = J_{\parallel 0} - \frac{1}{\mu_0} \nabla_\perp^2 \tilde{A}_\parallel, v_E = \frac{1}{B_0} (b_0 \times \nabla_\perp \Phi) \tag{8}$$

21 Here $\nabla_\parallel F = B \partial_\parallel (F/B)$ for any F, $\partial_\parallel = \partial_{\parallel 0} + \tilde{b} \cdot \nabla$, $\tilde{b} = \nabla \tilde{A}_\parallel \times b_0/B$, $\partial_{\parallel 0} = b_0 \cdot \nabla$,

22 $\kappa_0 = b_0 \cdot \nabla b_0$, ion pressure P_i and total pressure $P = P_i + P_e$. In Eq. (7), the second term in

23 perturbed vorticity equation includes the diamagnetic effect. Despite the simplification, this set

24 of reduced three-field modules has been successfully used in simulating ELM dynamics and

25 for gaining physics insight into both the ELM trigger and crash regime[37][38][39][40]. In our

26 nonlinear simulation, the equilibria used for calculation in BOUT++ are constructed as

27 described in Section 2 and are marginally unstable near the peeling ballooning boundary. The

28 simulation domain in the normalized poloidal flux is $0.8 < \psi_N < 1.1$ ($\rho = \sqrt{\psi_N}$), and the

grid resolution is $n_\psi = 132, n_y = 128, n_z = 33$, where y is the parallel coordinate and z is the toroidal angle. Similar to Ref.19, the radial boundary condition is set as $\widetilde{\varpi} = 0$, $\nabla_\perp^2 \widetilde{A_\parallel} = 0$, $\partial\tilde{p}/\partial\psi = 0$ and $\partial\tilde{\phi}/\partial\psi = 0$ on the outer boundary; $\widetilde{\varpi} = 0$, $\nabla_\perp^2 \widetilde{A_\parallel} = 0$, $\partial\tilde{p}/\partial\psi = -0.005$ and $\partial\tilde{\phi}/\partial\psi = 0$ on the inner boundary. Note that we have to adjust the inner boundary condition by increasing the perturbed pressure gradient to balance the convective term $\langle\tilde{v}_E\rangle \cdot \nabla P_0$ in Eq. (5), in order to maintain the pressure at the inner boundary approximately constant i.e. $\frac{\partial\langle\tilde{p}\rangle}{\partial t}$ ~0. We choose 1/5 and 1/3 of the torus to do the simulation for efficiency. As a result, only modes with multiples of n=5 or 3, respectively, will contribute to the simulation. Once we identify a dominant n mode number, the neighboring modes are likely to be unstable as well. They could be resolved by more careful study if needed. Density and temperature profiles of ion and electron along with the current and pressure profiles are all transformed to the BOUT++ grid file from the ONETWO gfile. Moreover, the local diamagnetic effect, which is not modeled in ELITE, is accounted for in BOUT++. This is especially important for high n ballooning modes.

Table 2. Three different collisionality cases around the CFETR pedestal peeling and ballooning boundary.

| Case name	Pedestal top density (10^{19}m^{-3})	Pedestal Height(kPa)	$J.B/B_0$ (10^4 A/m^2)	Alpha	ν_e^*	T_e(keV)
Case(a)	10	87.9	46.1	5.6	0.14	2.7
Case(b)	19	139.9	50.6	6.4	0.39	2.3
Case(c)	25	110.1	31.0	5.2	1.31	1.4

4.1 Exploring ELM dynamics along the peeling-ballooning boundary of CFETR

A schematic plot of plasma β_p versus normalized collisionality ν^* for defining the ELM types, constructed from an experimental database, is illustrated in Fig. 8. We note that for low β_p, such as in ITER, Type-I ELMs are expected for all collisionality. At high collisionality, both Type-II and Type-III ELMs can occur according to this dataset (As noted earlier, Type-III ELMs could occur over a broad range of collisionalities according to other experiments. Because they occur

1 below the ballooning stability limit, they typically have lower pedestal height). At higher β_p, a

2 grassy-ELM window appears with intermediate ν^* from 0.3 to 0.7. Even though experimental

3 data is absent for low and high ν^* at $\beta_p \sim 2$ or higher, we surmise that they would be in the Type-

4 I ELM or mixed-ELM regime based on extrapolation from around $\beta_p \sim 1.7$. More discussion of

5 the mixed-ELM regime will be presented in the next Section and also in Section 5. Using design

6 parameters, the β_p and ν^* of CFETR R=6.6m phase II baseline case are qualitatively in the

7 grassy-ELM region. An important task at hand is to quantitatively reproduce the grassy-ELM

8 window and to understand the physics to support the robustness of this window.
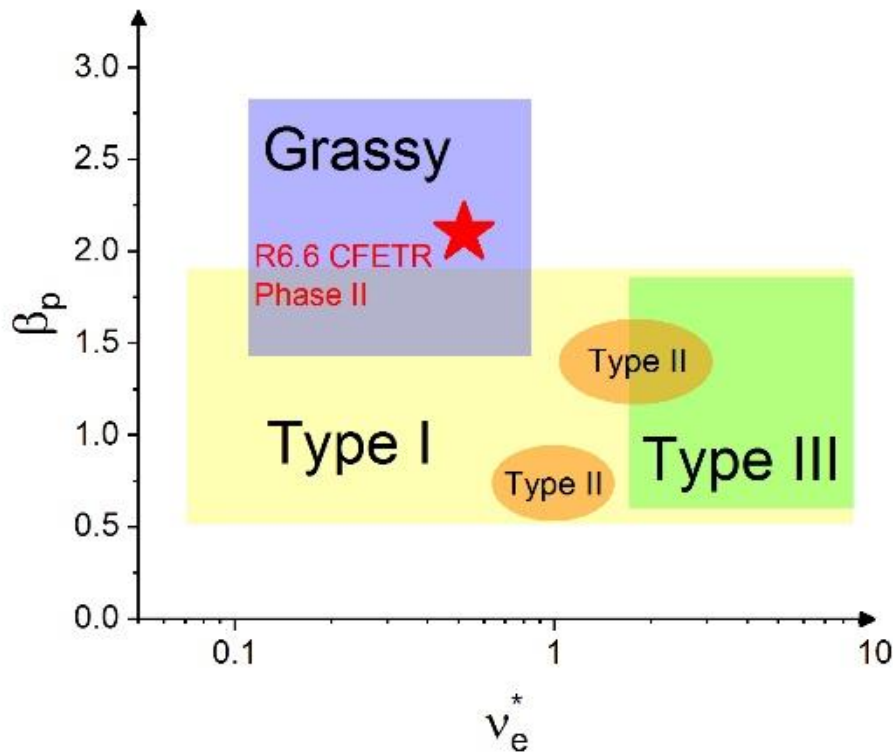

9

10 **Figure 8.** *A schematic plot of β_p versus normalized collisionality ν^* for defining the ELM type*

11 *based on experimental results [32][41]. The values of β_p and ν^* in the CFETR R=6.6m phase II*

12 *baseline case are around 2 and 0.5, respectively.*

13 *Case (A) Nonlinear ELM dynamics at low ν^**

14   This is the regime where both the kink-peeling drive and the ballooning drive are comparable,

15 and one cannot determine *a priori* which one is more dominant if at all. Fig. 9 shows the

16 nonlinear results of CFETR R=6.6m phase II with pedestal top density equals to $1 \times 10^{20} \text{m}^{-3}$,

17 corresponding to collisionality $\nu^*=0.14$, and electron temperature $T_e=2.74$ KeV. Initial pressure

1   and current profiles are shown in Fig. 9(a). As noted, the pedestal width is not particularly broad

2   because of the lower pedestal height, which could have an effect on the unstable mode width

3   and the nonlinear evolution as we shall see. Fig. 9(b) shows that after about 100 Alfvén times

4    $\tau_A(\tau_A=2*10^{-7}$ s), the linear phase ends and the RMS pressure at the steepest gradient location

5   reaches saturation. Details of the collapse are depicted in Fig. 9(c). The pressure profile firstly

6   collapses at the place where the pressure gradient and the current are largest. Then the collapse

7   spread to the inner boundary and the outer boundary. From 100 τ_A to 300 τ_A, energy is

8   transported from the inner pedestal to the scrape-off-layer (SOL), after which the decrease in

9   pedestal pressure starts to affect the core. All these features are common to Type-I ELM crash

10   observed in many tokamaks[42][43]. However, because of the high β_p (Shafranov shift) stabilizing

11   effect, the fraction of energy ejected relative to the pedestal energy W_{ped} (1.8% in Fig. 9(c))

12   might be at the lower end for Type-I ELM crash. Sometimes, this is referred to as the mixed-

13   ELM regime. Note that the pedestal collapse time of ~500 τ_A is significantly shorter than that

14   of experiments. Improvement in BOUT++ is needed in the future to quantify the temporal

15   dynamics of pedestal collapse.

16

1

2
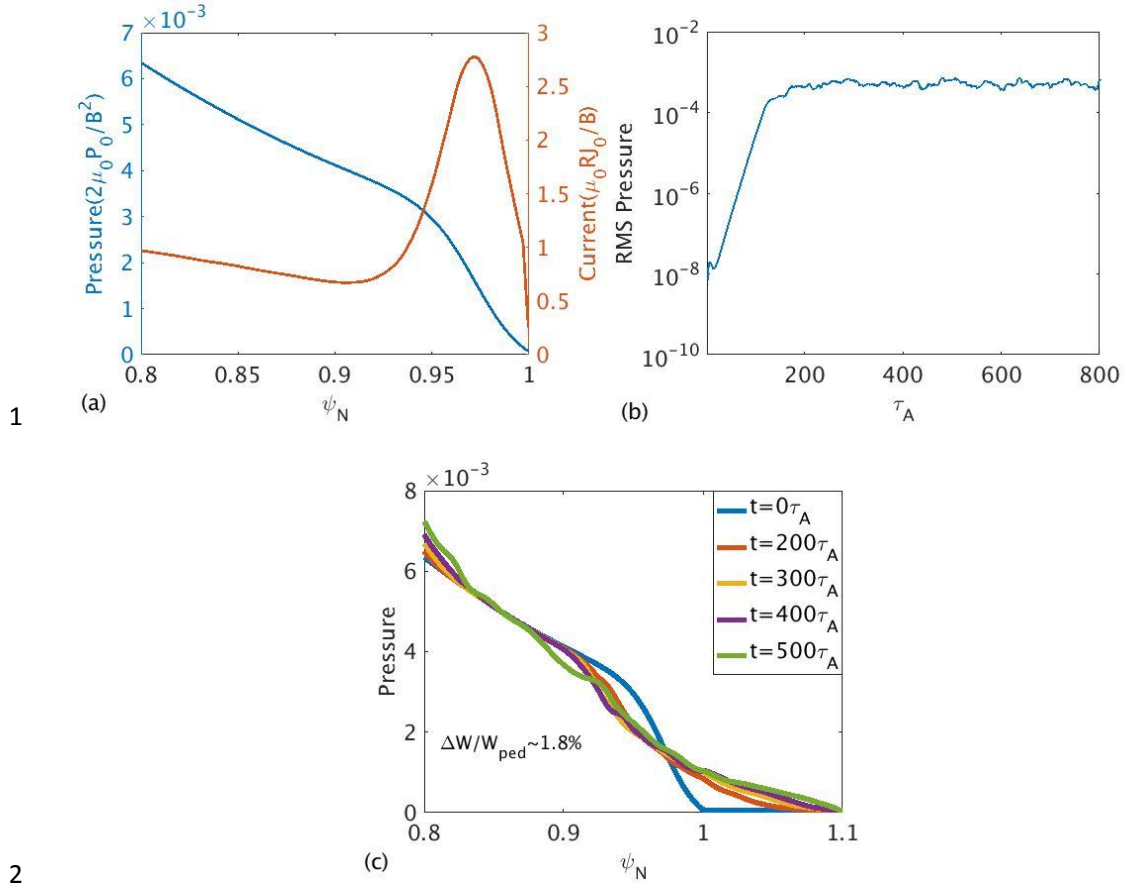
Figure 9. BOUT++ *nonlinear simulation of* $v^* = 0.14$ *CFETR R=6.6m phase II case: (a) Initial pressure and current profiles. The horizontal axis is* ψ_N *and* $\rho = \sqrt{\psi_N}$*; (b) Root mean squared (RMS) perturbed pressure at peak equilibrium gradient and outer midplane averaged along the z direction; (c) Pressure profile evolution at different time slices.*

To understand what causes the irreversible collapse, we examine the temporal evolution of the unstable modes and their nonlinear interaction. Fig. 10(a) shows that the most unstable mode during the linear phase of Type-I ELM activity is n=20. The higher n number is suggestive that the linear drive is from the pressure gradient at the steepest location, which is corroborated by its mode structure [Fig. 10(c)]. In the nonlinear phase, many unstable modes are excited [Fig. 10(b)]. Two features are noteworthy. First, the peak of the n=20 mode is at ψ_N=0.98 in its linear phase, whereas, the peaks of all the unstable modes have shifted inward to ψ_N~0.96. The flattening of the pressure gradient at ψ_N=0.98 by a narrow mode results in the steepening of the pressure gradient further inside [see Fig. 9(c)], which further destabilizes other neighboring modes. Second, the down cascade from high n to lower n modes is a common feature observed in other simulations[19]. The dominant n=5 mode in the nonlinear phase could

1 be driven by a combination of the pedestal pressure and current. The lower n modes are mainly

2 responsible for carrying the energy from the pedestal to the SOL[Fig. 10(d)-(f)]. As a check,

3 simulation using 1/3 of the torus shows that the n=3 mode is also unstable, indicating n=5 is

4 not a lower limit.
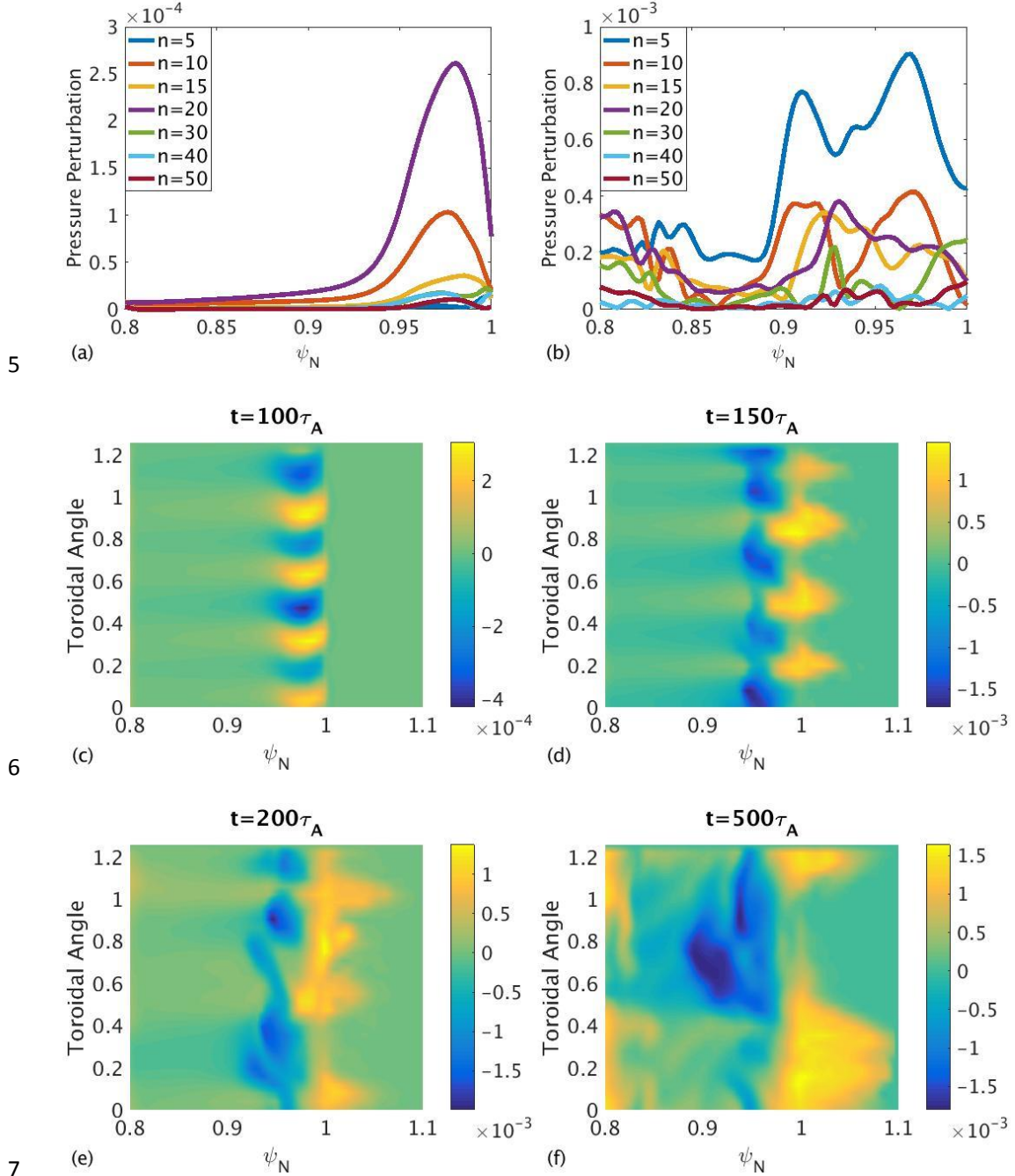
Figure 10. *Mode structures evolution and contour plot of perturbed pressure at the outer midplane of $v^* = 0.14$ CFETR R=6.6m phase II case: (a)-(b) Mode structure before and after nonlinear phase of toroidal number=5-50; (c)-(f) Contour plot of perturbed pressure at different time.*

1

2 *Case (B) Nonlinear ELM dynamics at intermediate v^**

3 This is the regime where we have established that kink-peeling is the dominant driving

4 mechanism from the linear analysis in Section 3. Fig. 11 describes the nonlinear results of

5 CFETR R=6.6m phase II with pedestal top density equals to $1.9 \times 10^{20} m^{-3}$, corresponding to

6 collisionality $v^* = 0.39$, and electron temperature $T_e = 2.3$ KeV. Initial pressure and current

7 profiles are shown in Fig. 11(a), and as expected the high pedestal height leads to a broader

8 pedestal width. The pedestal current is similarly wider suggesting that the pedestal current

9 rather than the current density gradient is the main driver of the instability[34]. Fig. 11 (b) and

10 (c) show that the RMS pressure reaches saturation and the perturbed pressure at the inner region

11 starts to decay at around 200 τ_A. This also supports the conjecture that the instability occurs

12 simultaneously across the entire pedestal, which can only happen for low-n mode with broad

13 mode width, i.e. kink-peeling mode. Little energy escapes from the pedestal to the SOL up to

14 450 τ_A, beyond which the pedestal energy fluctuations

15

16
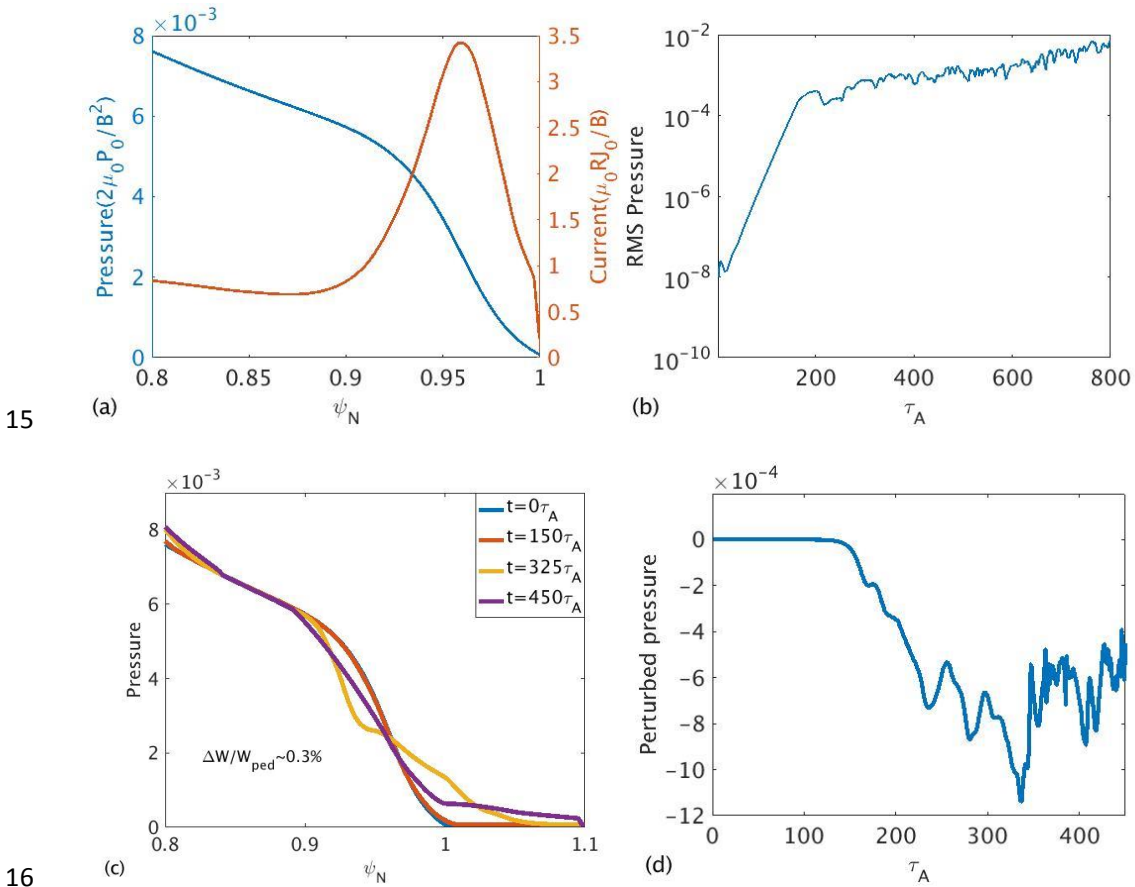
17 *Figure 11. BOUT++ nonlinear simulation of $v^* = 0.39$ case: (a) Initial pressure and current*

1   *profiles; (b) RMS perturbed pressure at peak equilibrium gradient and outer midplane*

2   *averaged along the z direction; (c) Pressure profile evolution at different time slices; (d)*

3   *Perturbed pressure profile evolution at $\Psi_n = 0.95$*

4   Notice that near $\Psi_n = 0.95$ in Fig. 11, the pressure drops to its lowest value around 325 τ_A

5   then starts to recover [Fig. 11 (d)]. To explain this apparent cyclic behavior, first, we note that

6   only a couple of lower n modes, namely n=10 and 5, are dominating the action throughout the

7   time span of the simulation [Fig. 12 (a) and (b)], and the mode widths are wider [Fig. 12 (c)

8   and (d)]. The intermediate and high n modes remain only mildly unstable. This is consistent

9   with modes being driven mainly by the pedestal current. Since our simulation is using only 1/5

10 sector, we cannot eliminate the possibility that modes with n between 5 and 10 are also

11 destabilized by mode-coupling. However, the large pedestal current results in a flat q_{ped} profile

12 (shown in Fig. 13), which increases the mode separation Δn ($\propto$ m/q') and makes it harder for

13 mode-mode coupling with decreasing n. Case (B) result suggests that the initially unstable n=10

14 mode triggers a dominantly unstable mode spectrum peaked around a lower n (e.g. n=5 in our

15 1/5 torus simulation), which is mainly responsible for ejecting the energy into the SOL [Fig.

16 12(e) and (f)]. It is thus reasonable to consider the behavior of a single dominant mode to

17 understand the cyclic behavior in the nonlinear evolution.

18 (a)   (b)
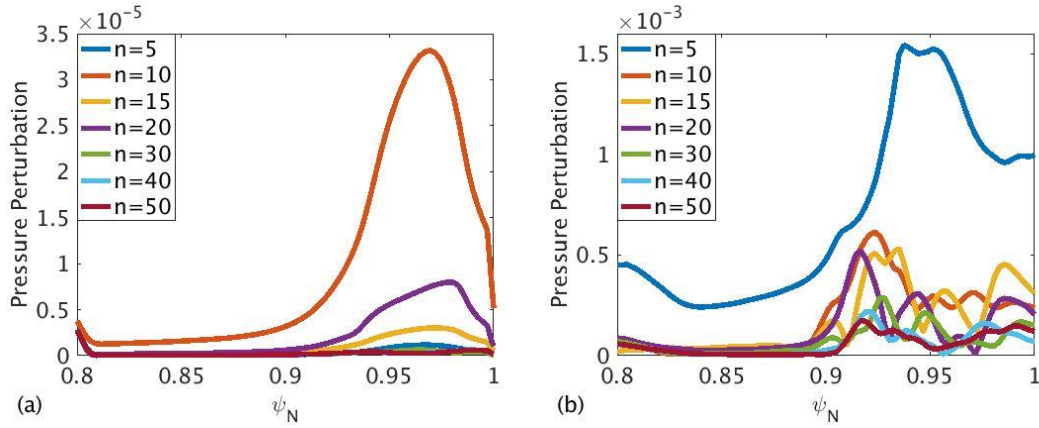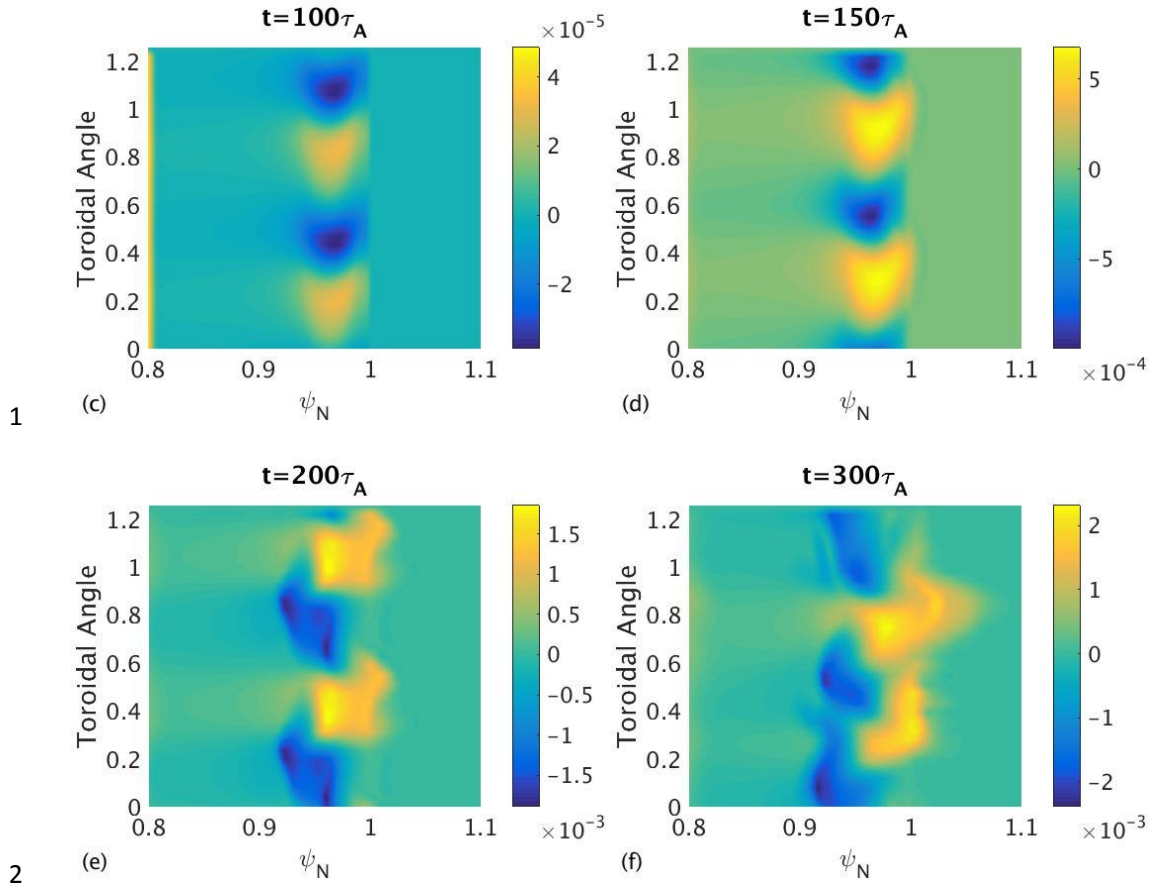
Figure 12. Mode structures evolution and contour plot of perturbed pressure at the outer midplane of $v^* = 0.39$ CFETR R=6.6m phase II case: (a)-(b) Mode structure before and after nonlinear phase of toroidal number=5-40; (c)-(f) Contour plot of perturbed pressure at different time.
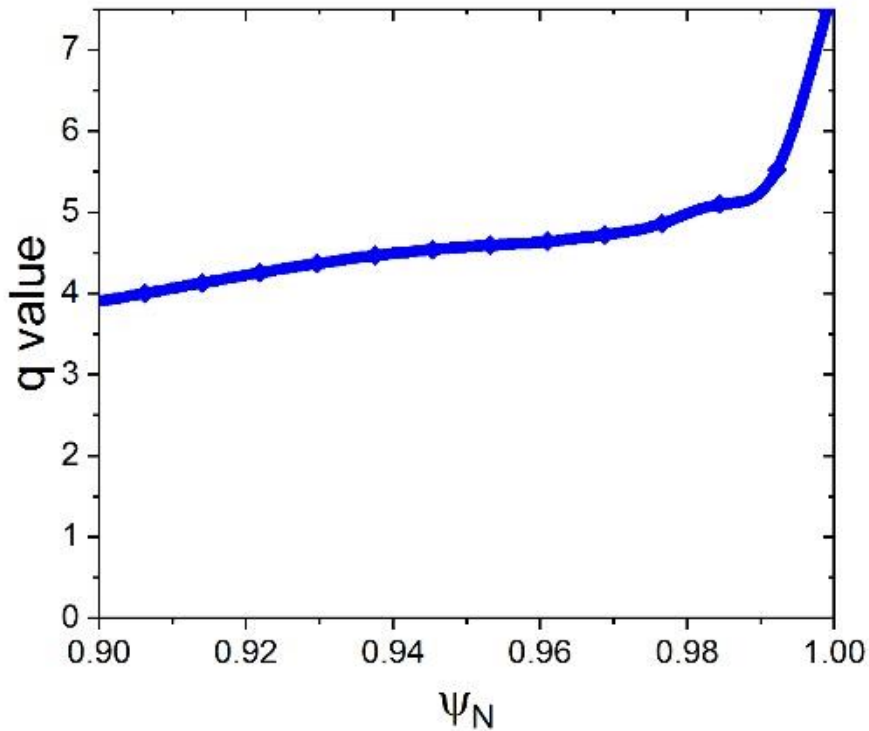
Figure 13. Flattening of the q_{ped} profile due to large I_{ped}.

The physics basis of the cyclic behavior for case (B) starts with the way the characteristic of the low n mode growth rate evolves as a function of the pedestal current with increasing β_p. Specifically, the growth rate acquires a sudden turn-on character at high β_p, i.e. it remains stable until a pedestal current threshold is reached, after which the instability grows explosively [see Fig.12 in Saarelma, et al Ref. 34]. The suppression of the growth rate below the threshold is due to the weakening of the $< \kappa \cdot \nabla P >$ drive from the increasing Shafranov shift at high β_p as discussed earlier. A similar plot of the growth rate versus pedestal current for the CFETR case is constructed in Fig.14. Let us start at a time when the pressure gradient is marginally stable. Since the pressure gradient is related to the current (in BOUT++, the two quantities are related by force balance, i.e. $\nabla p = JxB$), the current is sitting at the critical threshold. Any small perturbed pressure increase would lead to the pedestal current exceeding the threshold and the onset of an explosive instability. The latter would limit the current excursion from being too large before the pressure gradient is flattened, once again dropping the current below the threshold. The process would repeat itself, but the oscillation would never be large enough to lead to a complete collapse of the pedestal. Accordingly, the cyclic behavior would only occur

when kink-peeling drive dominates, i.e. in the intermediate ν^* window, which is the case when comparing the results of case (A), (B) and (C) . Lastly, it is important to note that the oscillation frequency of the simulation is significantly higher than the experimentally observed grassy-ELM frequency. We think this is because the Ohm's law used in this 3-field model does not properly include the Hall term, or (usually) finite electron mass terms. The former would introduce an ion skin depth effect, and finite electron mass would also tend to reduce oscillation frequencies.

A second and perhaps more convincing identifying feature of grassy-ELMs is the amount of energy ejected into the open field line region. We compute the ratios of the ejected energy $\Delta W = \int_{R_{in}}^{R_{out}} dR \oint d\theta (P_0 - \langle P \rangle_\zeta)$ across the separatrix (R_{in} is chosen as the inner boundary $\Psi_N = 0.8$ and R_{out} is at the separatrix $\Psi_N = 1.0$) to the initial pedestal energy $W_{ped} = \frac{3}{2} P_{ped} V_{plasma}$ for case (A) and (B). Note that the total plasma volume is used in the definition of W_{ped} following convention. The peak values of $\Delta W/ W_{ped}$ for both cases are indicated in fig. 9(c) and fig. 11(c), respectively. These plots clearly confirm that the ejected energy in case (B) ~0.3% is much smaller than that in case (A) ~1.8%, with the former within range of observations in experiments with grassy-ELMs. It also supports our argument that the explosive rise of the growth rate in case (B) acts to prevent a large excursion of the ELM amplitude. For case (B), we have further performed a sensitivity check on two critical parameters. First is the choice of inner boundary location. We moved the inner boundary to $\Psi_N = 0.75$ and confirmed that the value of $\Delta W/W_{ped}$ does not change. The second is the use of 1/5 torus to speed up the computation. In a much more time-consuming effort, $\Delta W/W_{ped}$ for full torus, 1/3 torus and 1/5 torus are obtained as 0.29%, 0.33% and 0.30%, respectively. This supports our argument that even though the low n mode spectra are different, as long as their growth rates possess the critical threshold characteristic (see Fig. 14), $\Delta W/W_{ped}$ will remain small.
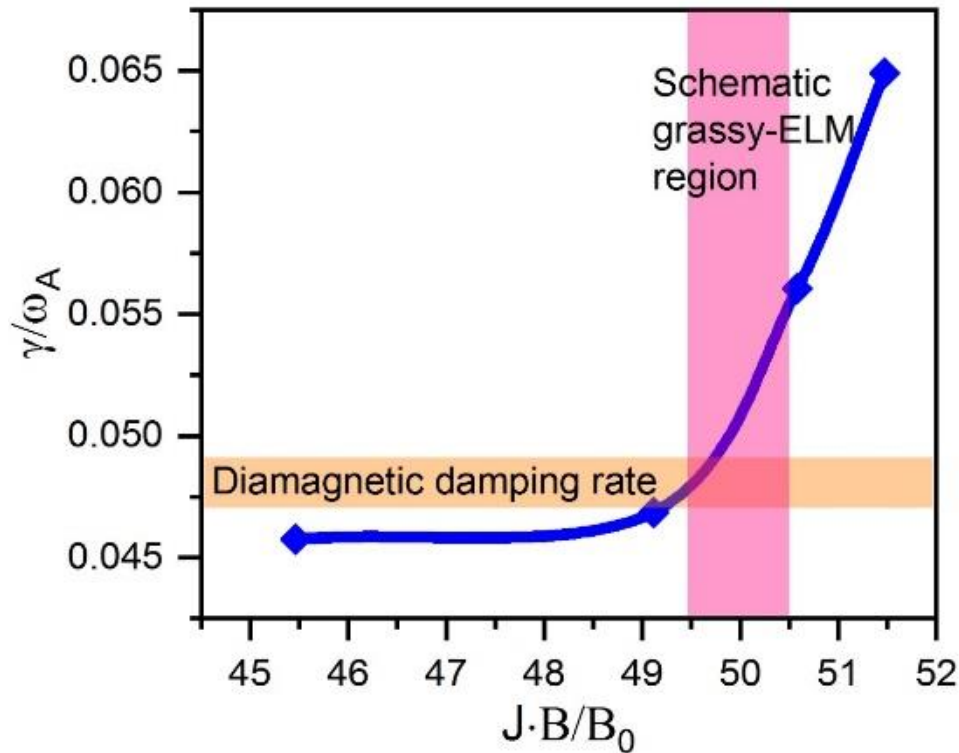
Figure 14. *Sudden turn-on character of the growth rate at high β_p for kink-peeling driven low-n mode (n=8)in CFETR.*

Case (C) Nonlinear ELM dynamics at high ν^*

This is the regime which is dominated by ballooning drive. Fig. 15 describes the nonlinear results of CFETR R=6.6m phase II with pedestal top density equals to $2.5 \times 10^{20} \text{m}^{-3}$, with corresponding collisionality $\nu^* = 1.31$. Because at higher density there is a transition from the peeling branch to the ballooning branch, the marginal stable point at this density has a much low temperature, which makes the collisionality of case (C) much larger than case (B). Fig. 15(a)-(d) display the same characteristics that fit with Type-I ELMs. The maximum value of $\Delta W/ W_{ped}$ for case (C) is 6.2% as indicated in Fig. 15(d). Again, the ratio is much larger than that for case (B) and is also several times larger than the value for case (A). Although both case(A) and case(C) share similar features of Type-I ELMs, there remains some detailed differences between case(A) and case(C), which warrant further studies in the future. For example, the peeling drive contribution could be more significant in case(A) than in case(C) because of the strong suppression of the bootstrap current at high collisionality.
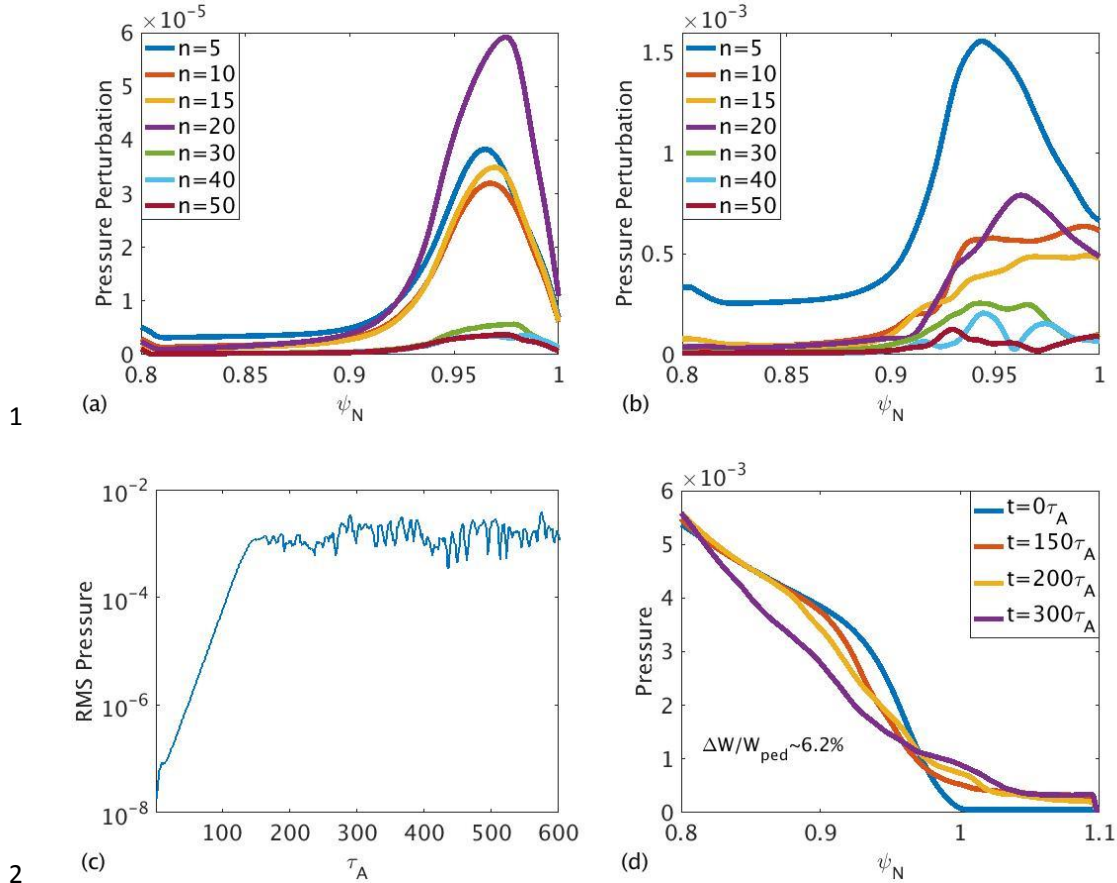
Figure 15. *Nonlinear calculation of $v^* = 1.31$ case: (a)-(b) Mode structure before and after nonlinear phase of toroidal number=5-50; (c) RMS perturbed pressure at peak equilibrium gradient and outer midplane averaged along the z direction; (d) Pressure profile evolution at different time slices.*

*4.2 Summary of ELM operation regimes on CFETR and dependence of ELM activities on triangularity*

Having demonstrated that there are at least three possibly different ELM behaviors that depend on collisionality along the CFETR pedestal stability boundary, we proceed to quantify the transition between regimes by carrying out simulations along the boundary in finer v^* grids. We confirmed that at $\beta_p \approx 2.0$, there is a robust grassy ELM window with v^* between 0.3-0.7, which is closely tied to high pedestal current and wide pedestal width [Fig. 16]. The grassy-ELM is driven by unstable kink-peeling modes with lower n numbers and characterized by a rapid oscillation/recovery that is roughly triangular in shape [Fig. 11(c)]. The ejected energy in a single crash $\Delta W/W_{ped}$ is very small (<<1%) [Fig. 17]. At v^* above and below the grassy-ELM

window, we also confirmed that the ELM behavior falls into the Type-I category. It is predominantly driven by ballooning modes with high n numbers and characterized by a sharp singular crash with a slow recovery. The ejected energy $\Delta W/ W_{ped}$ is an order of magnitude higher than the grassy-ELM regime [Fig. 17]. Our results are similar to the JT60-U experimental results (reported in fig. 2 of ref. 41) where grassy-ELMs highlighted in solid red dots appeared within a ν^* window. However, the existence of such a window was not mentioned in related JT60-U papers. They only stated that an upper ν^* limit existed for grassy-ELMs. It could be that their definition of a grassy-ELM was any ELM with $\Delta W/ W_{ped} < 1\text{-}2\%$. There is a big difference between ELMs with $\Delta W/ W_{ped} \sim 1\%$ and $\Delta W/ W_{ped} \sim 0.1\%$, regarding compatibility with wall erosion. We hope our paper would stimulate more new experiments to explore the existence and robustness of this window. It should be noted that Oyama, et al.[44] reported that plasma rotation profile was very different from the Type I ELMy plasmas and it was indeed possible to get both Type I and grassy ELMs with identical plasma pressure profiles, but different rotation profiles. Indeed, rotation has the effect of stabilizing high n (ballooning) modes and destabilizing low n (peeling) modes [45], which could make the latter more dominant leading to a grassy-ELM behavior. This aspect is not studied here. Our theory offers a different mechanism at high β_p with non-circular cross-section which results in the dominance of kink-peeling modes and a grassy ELM behavior. In large devices where beam-induced rotation is small, the high β_p mechanism might be more relevant. A systematic comparison with more recent experiments is described in Section 5.

1
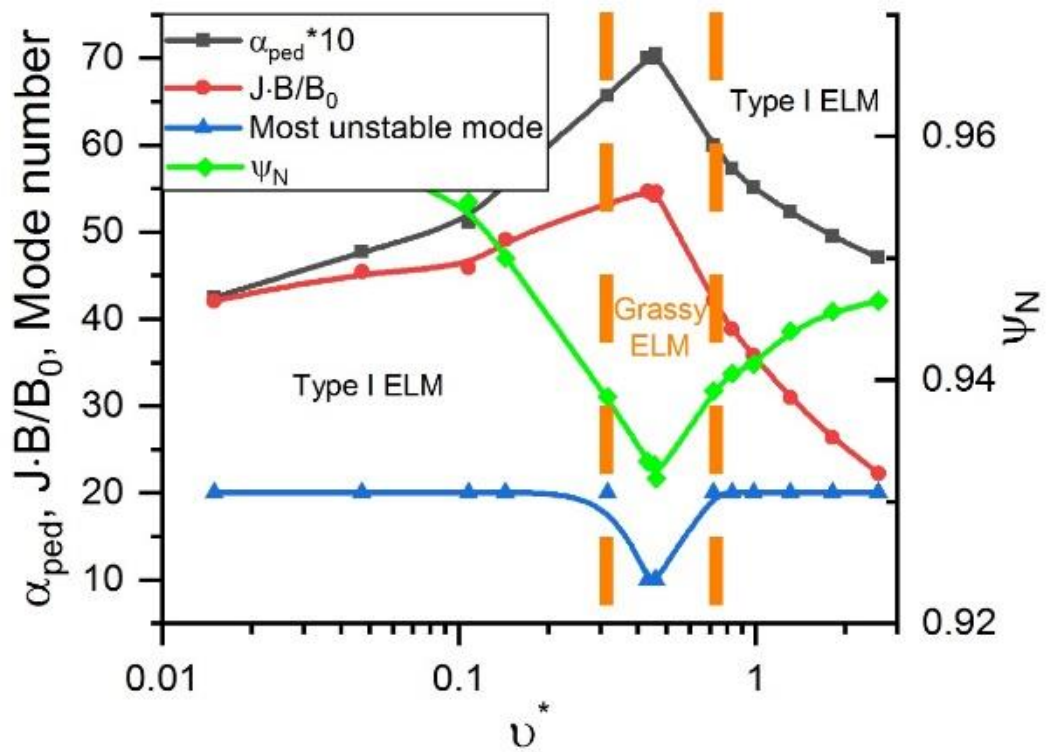
Figure 16. *Summary of ELM operation regimes and their distinguishing features along the*

marginal stability boundary of CFETR.
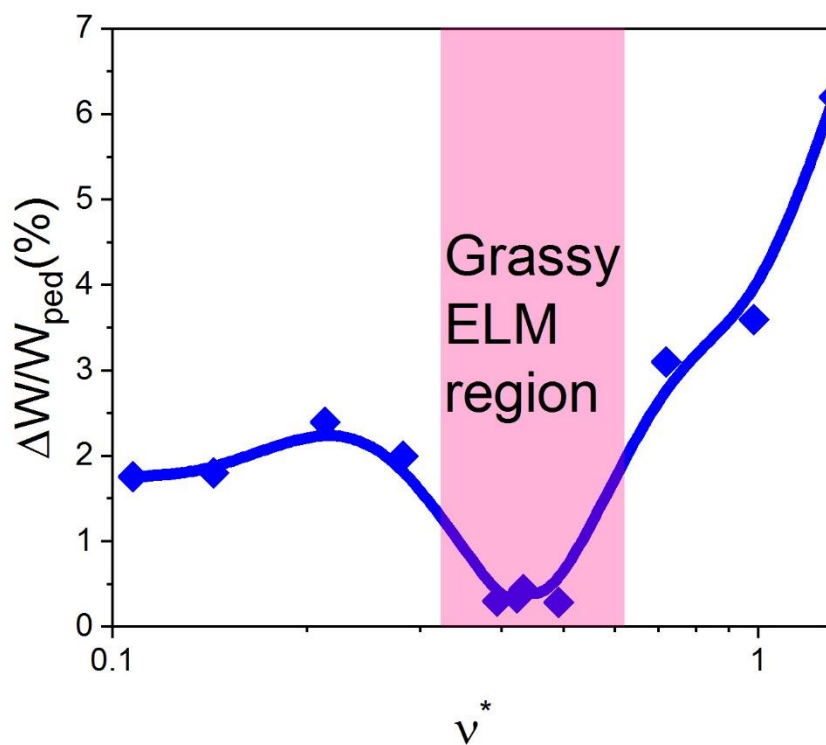
4

1 ***Figure 17.*** *Plot of energy loss of single ELM activity versus pedestal electron collisionality in*

2 *CFETR.*

3   Previously many papers have demonstrated the important role triangularity plays in

4 experimental steady state operation. With a higher triangularity, tokamak devices in general

5 achieve better pedestal performance[46]. Also Fig. 2(a) in Ref. 17 indicates that the access to

6 grassy-ELM needs either high triangularity or high q_{95}. They both reduce the growth rate but

7 the physics is different. High q_{95} produces high Shafranov shift that reduces the $< \kappa \cdot \nabla P >$

8 drive, which has been discussed extensively in our study. High triangularity results in reduced

9 bootstrap current, which diminishes the kink-peeling drive. This could be a reason why the

10 grassy-ELM window varies in different experiments[47] although it remains consistently in the

11 peeling branch. It is worthwhile to study it further in future.

12

13 **5.   Comparison of predicted ELM characteristics with experimental data**

14   Dependences of edge stability and ELM characteristics on various plasma parameters have

15 been studied extensively in experiments. Effects of plasma shape and pressure gradient on

16 ELMs are analyzed in Ref. 48. Stable ELM operation for ITER and other future fusion reactors

17 is still under study[15][49]. E. Viezzer has published a review of ELMs observed in many

18 tokamaks and categorized the characteristics of different ELMs[50]. Here we focus on a series

19 of experiments on the DIII-D tokamak[6][15][49][51]. In particular, five DIII-D discharges that cover

20 a broad range of β_p (0.6-2.2) and ν^* (0.06-6.0) have been surveyed to select specific time slices

21 where representative ELM behaviors are clearly identifiable [Fig. 18]. Equilibrium

22 reconstruction of these time slices are used to plot the marginally unstable PB mode boundary

23 using the code Varyped[52]; edge experimental data is used to locate the actual location of the

24 pedestal on the PB boundary; the energy loss for a single ELM crash $\Delta W/ W_{ped}$ is extracted for

25 each case; and finally, the most linearly unstable mode is calculated using ELITE. These results

26 are summarily displayed in Fig. 19.

27   As illustrated in Fig. 18, a grassy ELM case is clearly identifiable at intermediate ν^* and high

28 β_p by its rapid oscillations and a triangular shape in Dα signal, which are consistent with the

29 simulation results of CFETR case (B). A Type-I ELM identified by a very sharp burst of Dα

30 followed by a rapid decay is located at high β_p and high ν^*, consistent with the simulation results

1 of CFETR case (C). Moreover, only Type-I ELM discharges are found at low β_p, which supports

2 our theory that high β_p is responsible for suppressing the ballooning drive to create a grassy-

3 ELM window . Finally, at high β_p and low ν^*, the ELMs show a fast burst similar to Type-I

4 ELM. However, it exhibits a higher frequency and the amplitude could be small at times. We

5 associate this with the mixed-ELM regime, similar to what we found in CFETR case (A). This

6 regime is clearly influenced by ballooning modes but peeling modes might also play a role.
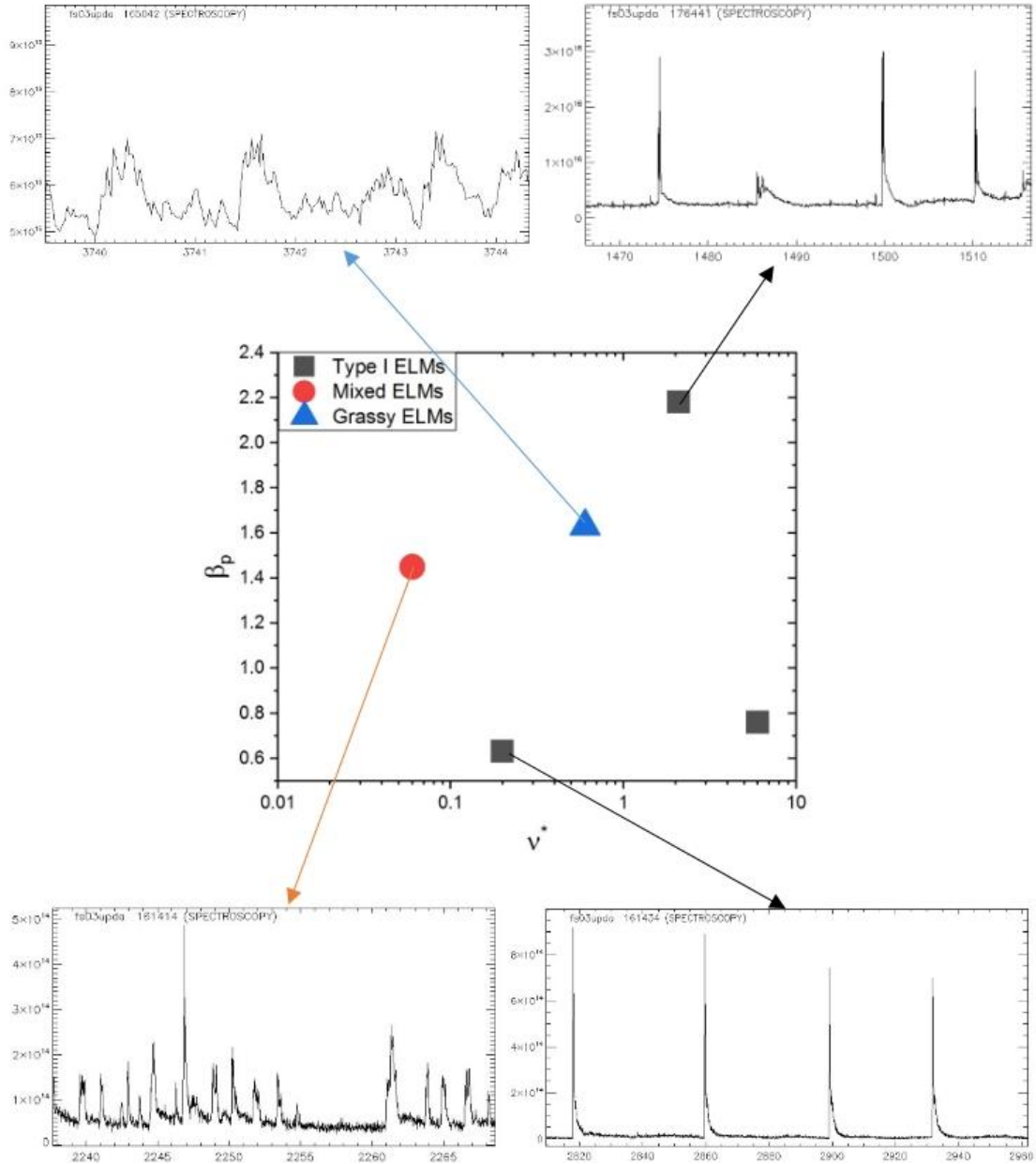

7

8

9 **Figure 18**. *Change of ELM character with β_p and ν^*. Triangle indicates a small amplitude*

10 *grassy ELM discharge, squares indicate discharges of giant Type-I ELMs and circle indicates*

a mixed-ELM regime.

2   Furthermore, we plot the peeling-ballooning boundaries and the locations of the pedestal for

3   the three high β_p ELM cases as well as one low β_p, low ν^* ELM case for comparison. As Fig.

4   19 shows, shot #161434 operate with Type-I ELMs, the dominant unstable toroidal mode is

5   n=20, and every single ELM activity causes large energy loss in the pedestal region (~25%).

6   Shots #161414, #165042 and #176441 are with high β_p, but they show very different ELM

7   activities. Shot #161414, with the pedestal located on the lower density side of the peeling

8   branch, shows mixed ELMs. The most unstable mode is a n=25 mode, and the energy loss due

9   to a single ELM activity is ~1.3%. Shot #165042 shows grassy ELMs, which cause very small

10   energy loss (~0.3%). The pedestal is located on the 'nose' part of the PB boundary, and the most

11   unstable mode is a low n mode (=10). Even though Shot #176441 shows giant Type-I ELMs,

12   with the pedestal on the ballooning branch and most unstable n=25, its energy loss from an

13   ELM crash is ~3.8%, which is much smaller than its low β_p cousins. The values of $\Delta W_{ELM}/W_{ped}$

14   computed by nonlinear BOUT++ simulations are displayed next to the experimental

15   measurements. Close agreement is obtained for the three high β_p cases . For the low β_p case, we

16   found that the giant Type I ELM crash affects the plasma much deeper into the core region, i.e.

17   the perturbation spreads further inward to the inner boundary (ψ_N=0.8) while $\Delta W_{ELM}/W_{ped}$

18   keeps on rising. Moving the inner boundary deeper increases $\Delta W_{ELM}/W_{ped}$. Since BOUT++ has

19   not been well-tested in modeling the core plasma, we can only draw a qualitative trend of

20    $\Delta W_{ELM}/W_{ped}$ rising to a much larger value (>12%) when compared with the high β_p cases,

21   consistent with the experimental numbers. It is obvious that β_p has a large stabilizing effect on

22   high n ballooning modes, so the discharges with high β_p always have a lower energy loss. This

23   could have led to some confusion that high β_p and low ν^* regime also supports grassy ELMs.

24   However, only the high β_p and intermediate ν^* window has the triangular shape of grassy ELMs

25   and very low energy loss due to the dominance of the kink-peeling mode. These experiments

26   correspond well to our CFETR simulation results, and comparison with JT-60U data[44] would

27   be worthwhile in the future.
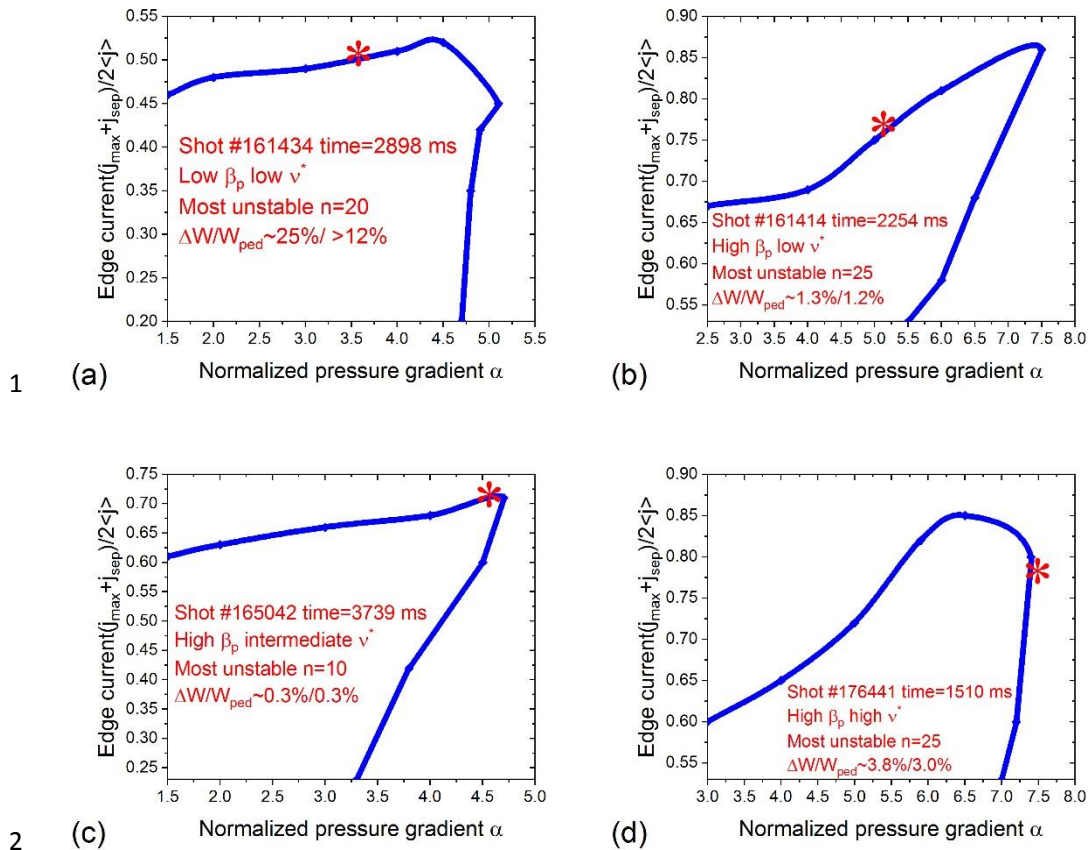
Figure 19. *Pedestal locations on the peeling-ballooning boundary as indicated by red stars for various ELMy discharges with different β_p and ν^*. $\Delta W / W_{ped}$ values (experimental /BOUT++ nonlinear simulation) are displayed side by side for comparison.*

Conclusion

Using a combination of linear and nonlinear analyses of self-consistently constructed equilibria, we have identified a robust grassy-ELM operation regime for future tokamak reactors, in particular the China Fusion Engineering Test Reactor (CFETR). The regime exists within a ν^* window at high β_p (e.g. ν^*=0.39, β_p=2.0), similar to results previously reported in experiments. A theoretical model that quantitatively explains the experimental features is presented for the first time. From a systematic scan of the pedestal density, EPED produces a marginal stability boundary to peeling-ballooning modes in I_{ped} versus α_{ped} space. The nonlinear simulation using BOUT++ along the stability boundary shows the instability varying from ballooning-dominated to peeling-dominated, then back to ballooning-dominated with increasing density. The change in density corresponds to a change in ν^* that affects the pedestal bootstrap current. High β_p leads to a strong Shafranov shift, which affects the flux surface averaged pressure drive. The two effects combine to create a peeling-dominated window in ν^*. Only the peeling-dominated regime shows a cyclic behavior during ELM crash, reminiscent of grassy-ELM dynamics. The ejected energy across the separatrix normalized to the initial pedestal energy is demonstrably smaller in the simulated grassy-ELM regime. The quick

recovery of the ELM crash is explainable by the rapid onset of low n kink-peeling instability when I_{ped} exceeds a threshold at high β_p, which is absent in the ballooning-dominated regime. The ELM characteristics of five DIII-D discharges that cover a range of β_p and ν^* are used to compare with our simulation predictions of the ELM shape and frequency, the most unstable toroidal n mode that identifies a peeling or ballooning dominated regime, and the relative energy loss in an ELM crash. The comparison fully supports our conclusion of the existence of a robust grassy-ELM regime at high β_p and an intermediate ν^* window. As a footnote, we should clarify that the Type-I ELM discussed in this paper follows the classification in Ref 44. However, this classification might not be universal in the literature. Some papers might define Type-I ELMs exclusively as giant ELMs with $\Delta W_{ELM}/W_{ped}$ much greater than 10%. Irrespective of the definition, our paper shows that Type-I ELMs are driven by ballooning modes. It is distinguished from the grassy-ELMs discussed, which are driven by peeling modes.

Grassy-ELM operation is desirable for future tokamak reactors such as CFETR, because of a lower transient heat flux to the first wall and a beneficial impurity cleansing effect. Operation in the grassy-ELM window also constrains the density in the core and the SOL, which has to be accounted for self-consistently in the physics design of future reactors. Much more study of small ELMs or ELM-free operation is needed. Quiescent H-mode is another possible candidate for CFETR steady-state operation and its physics is still not well-understood. Super H-mode and the second stable region are also promising topics for research. New experiments and further development of the BOUT++ framework and EPED model should facilitate these investigations.

of the National Magnetic Confinement Fusion Program of China under Contract No. 2015GB111001. Numerical computations were performed on the CFETR cluster in the Supercomputing Center of University of Science and Technology of China, and the NERSC cluster in the U.S.

References

[1] Y. Wan 2016 Overview of the Present Progresses and Activities on the Chinese Fusion Engineering Test Reactor 26th IAEA FUSION ENERGY CONFERENCE OV/3-4

[2] Aymar R., Barabaschi P. and Shimomura Y. 2002 The ITER design Plasma Phys. Control. Fusion 44 519

[3] G. Zhuang 2018 Progress of the CFETR Design 27th IAEA FUSION ENERGY CONFERENCE OV/3-2

[4] H. Zohm 1996 Edge localized modes(ELMs) Plasma Phys. Control. Fusion 38 105

[5] Evans T.E. et al 2006 Edge stability and transport control with resonant magnetic perturbations in collisionless tokamak plasmas Nat. Phys. 2 419-23

[6] R. Nazikian et al 2018 Grassy-ELM regime with edge resonant magnetic perturbations in fully noninductive plasmas in the DIII-D tokamak Nucl. Fusion 58 106010

[7] L.R. Baylor et al 2016 Pellet Injection Technology and Its Applications on ITER IEEE TRANSACTIONS ON PLASMA SCIENCE, VOL. 44, NO. 9, SEPTEMBER 2016

[8] A Loarte, G Saibene, R Sartori, D Campbell et al 2003 Characteristics of type I ELM energy and particle losses in existing devices and their extrapolation to ITER Plasma Phys. Control. Fusion 45 1549-1569

[9] J.W. Connor 1998 Edge-localized modes—physics and theory Plasma Phys. Control. Fusion 40 531-542

[10] B. Labit et al. 2018 Plasma shape and fueling dependence on the small elms regime in TCV and AUG 27th IAEA FUSION ENERGY CONFERENCE EX/2-5

[11]N Oyama et al 2006 Pedestal conditions for small ELM regimes in tokamaks Plama Phys. Control. Fusion 48 A171

[12] Stober J et al 2001 Type II ELMy H modes on ASDEX Upgrade with good confinement at high density Nucl. Fusion 41 1123

[13] Saibene G et al 2002 Improved performance of ELMy H-modes at high density by plasma shaping in JET Plasma Phys. Control. Fusion 44 1769

[14] R. Sartori, G. Saibene, L. D. Horton et al. 2004 Study of Type III ELMs in JETs Plasma Phys. Control. Fusion 46 723-750

[15] A. M. Garofalo, W. M. Solomon, J.-K. Park et al 2011 Advances towards QH-mode

viability for ELM-stable operation in ITER Nucl. Fusion 51 083018

[16] T Happel, M Griener, D Silvagni et al. 2018 Advances in the understanding of the I-mode confinement regime: access, stationarity, edge/SOL transport and divertor impact 27th IAEA Fusion Energy Conference

[17] N. Oyama et al 2010 Effects of edge collisionality on ELM characteristics in the grassy ELM regime Nucl. Fusion 50 064014

[18] Jiale Chen et al 2017 Self-consistent modeling of CFETR baseline scenarios for steady-state operation Plasma Phys. Control. Fusion 59 075005

[19] Ze-Yu Li, V.S. Chan. et al 2018 Ideal MHD stability and characteristics of edge localized modes on CFETR Nucl. Fusion 58 016018

[20] P.B. Snyder, H.R. Wilson et al 2004 ELMs and constraints on the H-mode pedestal: peeling-ballooning stability calculation and comparison with experiment Nucl. Fusion 44 320-328

[21] O. Meneghini, P.B. Snyder. et al 2016 Integrated fusion simulation with self-consistent core-pedestal coupling Physics of Plasmas 23,042507

[22] P.B. Snyder. et al 2009 Pedestal stability comparison and ITER pedestal prediction Nucl. Fusion 49 085035

[23] P.B. Snyder et al 2009 Development and validation of a predictive model for the pedestal height Physics of Plasmas 16,056118

[24] P.B. Snyder et al 2011 A first-principles predictive model of the pedestal height and width: development, testing and ITER optimization with the EPED model Nucl.Fusion 51 103016

[25] R.L. Miller, J.W. Van Dam 1987 Hot particle stabilization of ballooning modes in tokamaks Nucl. Fusion 27 2101

[26] P.B. Snyder, H.R. Wilson. et al 2004 ELMs and constraints on the H-mode
pedestal: peeling–ballooning stability calculation and comparison with experiment Nucl.Fusion 44 320-328

[27] Orso Meneghini and Lang Lao, 2013, Integrated Modling of Tokamak Experiments with OMFIT, Plasma and Fusion Research: Regular Articles, Volume 8, 2403009.

[28] J. Candy, C. Holland, R.E. Waltz et al 2009 Tokamak profile prediction using direct gyrokinetic and neoclassical simulation, Physics of Plasmas 16, 060704

[29] W.W. Pfeiffer et al 1980 ONETWO: a computer code for modeling plasma transport in tokamaks General Atomics Company, GA A16178, San Diego

[30] L.L. Lao et al 1985 Reconstruction of current profile parameters and palsma shapes in tokamaks Nucl. Fusion 25 1611

[31] Yuanxi Wan, Jiangang Li et al. 2017 Overview of the present progress and activities on the CFETR Nucl. Fusion 57 102009

[32] Oyama N. 2008 Progress and issues in understanding the physics of ELM dynamics, ELM

mitigation, and ELM control J. Phys.: Conf. Ser. 123 012002

[33] P.B. Snyder et al 2015 Super H-mode: theoretical prediction and initial observations of a new high performance regime for tokamak operation Nucl. Fusion 55 083026

[34] S. Saarelma and S.Gunter. 2004 Edge stability analysis of high βp plasmas Plasma Phys.Control.Fusion 46 1259-1270

[35] P.B. Snyder, H.R. Wilson et al. 2002 Edge localized modes and the pedestal: A model based on coupled peeling–ballooning modes Physics of Plasmas 9, 2037

[36] X.Q.Xu, B.D.Dudson. et al 2011 Nonlinear ELM simulations based on a nonideal peeling–ballooning model using the BOUT++ code Nucl. Fusion 51 103040

[37] Xi P.W. et al 2013 Impact of a large density gradient on linear and nonlinear edge-localized mode simulations Nucl. Fusion 53 113020

[38] Xi P., Xu X. and Diamond P. 2014 Phase dynamics criterion for fast relaxation of high-confinement-mode plasmas Phys. Rev. Lett. 112 085001

[39] Xi P., Xu X. and Diamond P. 2014 The impact of pedestal turbulence and electron inertia on edge-localized-mode crashes Phys. Plasmas 21 056110

[40] Xu X. et al 2013 Gyro-fluid and two-fluid theory and simulations of edge-localized-modes Phys. Plamsas 20 056113

[41] Oyama N. 2006 Pedestal conditions for small ELM regimes in tokamaks Plasma Phys. Control. Fusion 48 A171–81

[42] A Loarte et al. 2003 Characteristics of type I ELM energy and particle losses in existing devices and their extrapolation to ITER Plasma Physics and Controlled Fusion 45 1549-1569

[43] T. Kass et al. 1998 Characteristics of type I and type III ELM precursors in ASDEX upgrade Nucl. Fusion 38 111

[44] N. Oyama, Y. Sakamoto, A. Isayama, M. Takechi, P. Gohil et al 2005 Energy loss for grassy ELMs and effects of plasma rotation on the ELM characteristics in JT-60U Nucl. Fusion 45 871

[45] P. W. Xi, X. Q. Xu, X. G. Wang and T. Y. Xia 2012 Influence of equilibrium shear flow on peeling-ballooning instability and edge localized mode crash Physic of Plasmas 19, 092503

[46] S.K.kim et al 2018 Dependence of pedestal properties on plasma parameters Nucl. Fusion 58 016036

[47] G. S. Xu 2018 A Promising Grassy ELM Regime for High-Performance Steady-State Operations with Metal Wall in EAST and CFETR 27th IAEA FUSION ENERGY CONFERENCE EX/P2-4

[48] L. L. Lao, Y. Kamada, T. Oikawa et al 2001 Dependence of edge stability on plasma shape and local pressure gradients in the DIII-D and JT-60U tokamaks Nuclear Fusion, Vol. 41, No. 3

[49] A. M. Garofalo et al 2015 Compatibility of internal transport barrier with steady-state

operation in the high bootstrap fraction regime on DIII-D Nucl. Fusion 55 123025

[50] E. Viezzer 2018 Access and sustainment of naturally ELM-free and small-ELM regimes Nucl. Fusion 58 115002

[51] R.A. Moyer, C. Paz-Soldan, R. Nazikian, D.M. Orlov, N.M. Ferraro et al 2017 Validation of the model for ELM suppression with 3D magnetic fields using low torque ITER baseline scenario discharges in DIII-D Phys. Plasmas 24 102501-1

[52] T. H. Osborne, P. B. Snyder, K. H. Burrell et al Edge stability of stationary ELM-suppressed regimes on DIII-D General Atomics Report GA-A25943